Modelling of coupled cross-flow and in-line vortex-induced vibrations of flexible cylindrical structures
Part II: on the importance of in-line coupling

Qu, Yang; Metrikine, Andrei V.

Important note
To cite this publication, please use the final published version (if applicable).
Please check the document version above.

Modelling of coupled cross-flow and in-line vortex-induced vibrations of flexible cylindrical structures. Part II: On the importance of in-line coupling

Yang Qu · Andrei V. Metrikine

Abstract To illustrate the influence of the in-line coupling on the prediction of vortex-induced vibration (VIV), the simulation results of the coupled cross-flow and in-line VIVs of flexible cylinders - obtained with three different wake oscillator models with and without the in-line coupling- are compared and studied in this paper. Both the cases of uniform and linearly sheared flow are analysed and the simulation results of the three models are compared with each other from the viewpoints of response pattern, fluid force, energy transfer and fatigue damage. The differences between the simulation results from the three models highlight the importance of the in-line coupling on the prediction of coupled cross-flow and in-line VIVs of flexible cylindrical structures.

1 Introduction

Vortex-induced vibration (VIV) is a well-known phenomenon to civil engineers as they often occur in flexible cylindrical structures, such as chimneys, cables of suspended bridges, suspended power lines, offshore risers and mooring cables, that are subjected to air or water flows. The possible fatigue damage resulting from

Y. Qu (Corresponding author) and A.V. Metrikine
Department of Hydraulic Engineering, Delft University of Technology, Stevinweg 1, 2628CN Delft, The Netherlands

Present address of Y. Qu
State Key Laboratory of Ocean Engineering, Shanghai Jiao Tong University, Shanghai, 200240, China
E-mail: yangqu@sjtu.edu.cn

VIV requires a reliable and efficient prediction of VIV for the safety design of these structures.

In the early studies on the prediction of VIV, the focus has been placed on the cross-flow vibration and the influence of the in-line motion is normally ignored. However, it has been known, from experiments by Jauvtis [1] and Dahl [2], that the presence of the in-line motion may significantly change the wake pattern and consequently influence the cross-flow hydrodynamic forces and therefore cross-flow response. The same experiments have also revealed that certain motion trajectories, defined by a range of phase differences between cross-flow and in-line vibrations, are favourable for the large amplitude VIV. This implies that the motion trajectory, in addition to the reduced velocity and cross-flow amplitude, plays an important role in the energy transfer between the structure and fluid for the coupled cross-flow and in-line VIV [3–5]. Consequently, a tension dominated flexible structure undergoing VIV will tend to vibrate in the form of travelling wave in both cross-flow and in-line directions such that the motion trajectories that are favourable for VIV can persist over a larger segment of the structure compared to the case of standing wave [6].

Taking the effect of coupled cross-flow and in-line vibrations on the dynamics of the wake into account for the prediction of VIV has been a long standing issue. The widely used empirical codes, like VIVANA and SHEAR7, are still limited to handle the cross-flow and in-line vibrations separately. The difficulties associated with building a hydrodynamic force database that covers a wide range of combined cross-flow and in-line vibrations with high resolution have prevented these empirical methods from being extended to predict the coupled cross-flow and in-line VIV [7]. The wake oscillator model is another type of VIV model that has gained

popularity in recent years due to its low computational effort and acceptable accuracy. Although the classic wake oscillator model also only deals with the cross-flow VIV, it can be easily extended to predict the coupled cross-flow and in-line VIV by introducing a second wake oscillator equation to model the effect of the in-line motion on the fluctuating drag force in addition to the one that describes the relation between the lift force and cross-flow response [8, 9]. This approach, although captures some features of VIV, is not entirely consistent with the fact that the lift and drag forces have the same origin, i.e., the dynamics of the wake, and are interdependent on each other. It is physically more reasonable to use only one oscillator to describe the dynamics of the wake, and this oscillator should be coupled to both cross-flow and in-line vibrations. In line with this principle, Qu and Metrikine [10] have developed a new single wake oscillator model for coupled cross-flow and in-line VIVs of rigid cylinders and later applied it to flexible cylinders (Part I, submitted). In this new model, the in-line coupling is considered in two aspects. The first one is that a nonlinear in-line motion coupling term, in addition to the classic linear cross-flow acceleration coupling [11], is introduced in the wake oscillator equation. The second one is that a fluctuating in-line force, in coupling with the lift, is introduced in the equations of motion of the structure. With this in-line coupling, the new model has been shown to be able to capture important features of the coupled cross-flow and in-line VIV of an elastically supported rigid cylinder [10].

It needs to be pointed out that there are other studies which have also used the model that contains only one wake oscillator equation to simulate coupled cross-flow and in-line VIVs of flexible cylinders, e.g., the work by Mina [12] and Bai [13]. The former one uses exactly the same model by Ogink and Metrikine [14] which is a reduced formation of the model by Qu and Metrikine [10] when the two aspects of the in-line coupling described above are both excluded. The later one, on the other hand, ignores the in-line motion coupling term in the wake oscillator equation and only introduces a fluctuating in-line force that is coupled to the lift, i.e., the second aspect of the in-line coupling. According to [12] and [13], both models seem to predict coupled cross-flow and in-line VIVs of flexible cylinders with satisfactory results. However, as will be presented in this paper, both aspects of the in-line coupling is essential and necessary for the correct modelling of coupled cross-flow and in-line VIVs of flexible cylindrical structures.

The present paper focuses on quantifying the effects of the previously mentioned in-line coupling on the modelling of the coupled cross-flow and in-line VIV.
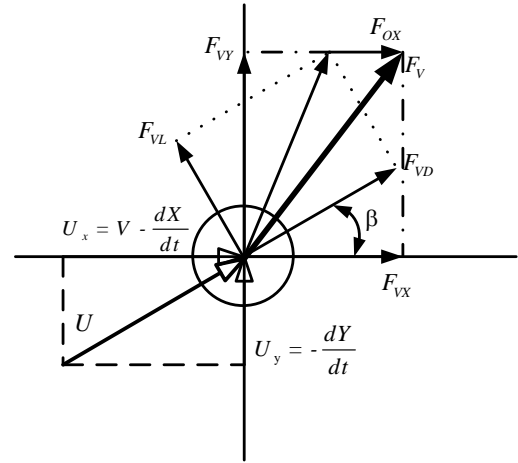

Fig. 1: Decomposition of the vortex force in drag, lift, cross-flow and in-line directions

To achieve this goal, simulations of the VIV of a flexible cylinder subjected to both uniform and linearly sheared flows are conducted using different models with and without the in-line coupling. The importance of the in-line coupling is highlighted by comparing the simulation results of these models with respect to response pattern, fluid force, energy transfer and fatigue damage. The reminder of this paper is structured as follows. The models, including the wake oscillator model, in-line couplings and structural model, are briefly described in Section 2. Then, in Section 3, the general structural responses obtained from the three models are presented. A 2D spatial-temporal spectral analysis is carried out, and vibration modes are extracted at dominant frequencies. Section 4 investigates the phase difference between the cross-flow and in-line motions. In Section 5, the differences between the results from the three models are highlighted from the viewpoint of energy transfer. The fatigue damage estimated by the three models is presented in Section 6, and final conclusions are provided in Section 7.

2 Model description

In this section, the wake oscillator model, in-line couplings as well as the structural model are briefly described.

2.1 Wake oscillator model and in-line coupling

Considering a case where the cylinder is rigid and the flow (with velocity V) is perpendicular to its axis, the

total vortex force F_V acting on the cylinder is decomposed into lift (F_{VL}), drag (F_{VD}) and fluctuating in-line (F_{OX}) forces; see Fig.1. The F_{VL} and F_{VD} are assumed to be perpendicular to and aligned with the relative flow velocity U. The F_{OX} is introduced in the in-line direction to account for the fluctuating nature of the in-line force. The magnitude of lift and drag forces per unit length are related to the relative flow velocity U and are defined as

$$F_{VL} = \frac{1}{2}\rho DU^2 C_{VL}, \quad F_{VD} = \frac{1}{2}\rho DU^2 C_{VD} \qquad (1)$$

where ρ is the mass density of the fluid, D is the diameter of the cylinder, C_{VL} and C_{VD} are lift and drag force coefficients respectively. The relative flow velocity is expressed as

$$U = \sqrt{\left(V - \frac{\mathrm{d}X}{\mathrm{d}t}\right)^2 + \left(\frac{\mathrm{d}Y}{\mathrm{d}t}\right)^2} \qquad (2)$$

where X and Y are the displacements of the cylinder in in-line and cross-flow directions respectively.

The F_{OX} is coupled to the lift force, following the relation between fluctuating lift and drag forces acting on a fixed cylinder [15], as

$$F_{OX} = \frac{1}{2}\alpha C_{VL}^2 \rho D |U_x| U_x, \qquad (3)$$

where α is an empirical parameter and $U_x = V - \mathrm{d}X/\mathrm{d}t$ is the relative flow velocity in the in-line direction.

To satisfy the hydrodynamic forces measured on a fixed cylinder, the values of α and C_{VD} are calculated as

$$\alpha = 2\frac{C_{D0}}{C_{L0}^2} \qquad (4)$$

and

$$C_{VD} = \overline{C}_D - \frac{1}{2}\alpha C_{L0}^2 \qquad (5)$$

where $\overline{C}_D$, C_{D0} and C_{L0} are mean drag, fluctuating drag and fluctuating lift force coefficients measured on a fixed cylinder. In this paper, $\overline{C}_D = 1.2$, $C_{D0} = 0.1$ and $C_{L0} = 0.3$, which are the same as those in [10], are adopted.

The dynamics of the wake is modelled by a van der Pol nonlinear equation which is coupled to both the cross-flow and in-line motions of the cylinder. The equation is given as

$$\frac{\mathrm{d}^2 q}{\mathrm{d}t^2} + \epsilon\omega_s(q^2-1)\frac{\mathrm{d}q}{dt} + \omega_s^2 q - \kappa\frac{\omega_s^4 D\frac{\mathrm{d}^2 X}{\mathrm{d}t^2}}{\omega_s^4 D^2 + \left(\frac{\mathrm{d}^2 X}{\mathrm{d}t^2}\right)^2}q = \frac{A}{D}\frac{\mathrm{d}^2 Y}{\mathrm{d}t^2} \qquad (6)$$

where q is the wake variable; ϵ, A and κ are tunning parameters; $\omega_s = 2\pi V \mathrm{St}/D$ is the Strouhal frequency and St is the Strouhal number. The values $\epsilon = 0.08$, $A = 8$, $\kappa = 5$ and $\mathrm{St} = 0.2$ from [10] are adopted in this paper. The lift force coefficient C_{VL} is associated with the wake variable q as

$$C_{VL} = \frac{q}{2}C_{L0} \qquad (7)$$

Representing the interaction between the fluid and the structure using an equivalent nonlinear oscillator, as given by Eq.(6), is the most important feature of the wake oscillator model. Without modelling the real flow field, the computational cost is significantly reduced while the main features of the VIV are still captured. From this viewpoint, the model presented in this paper is appropriate for the qualitative study of different VIV phenomena. However, this simplification also introduces some limitations. For example, the influence of the Reynolds number on the flow field is not considered and the three dimensional flow effect is also not included. The model, in its present form, only gives quantitative predictions of VIV in certain situations. This actually is a common limitation of all existing VIV prediction models due to the extremely complex flow field involved in the problem of VIV. The proposed model should be used with caution in practical applications where the quantitative prediction of VIV is important.

Compared to the classic models where only the cross-flow coupling between the structure and wake oscillator is considered, the model described above also contains an in-line coupling. This in-line coupling is introduced through an in-line motion coupling term in the wake oscillator equation and a fluctuating in-line force that is coupled to the lift in the structure's equations of motion. In order to investigate the effect of the in-line coupling, simulations are conducted with different models. Model A denotes the complete model, which includes both in-line coupling terms. Model B excludes the in-line motion coupling term in the wake oscillator equation but keeps the fluctuating in-line force, i.e., $\kappa = 0$; this is similar to the model by Bai [13]. Model C excludes both terms, i.e., $\kappa = 0$ and $\alpha = 0$, and is exactly the same as the one proposed by Ogink and Metrikine [14]. The simulation results of these models will be compared to each other and the influence of the in-line coupling will be investigated in Sections 3-6.

2.2 Structural model

In this paper, the models are used to simulate the VIV experiments undertaken by Shell Oil Company in the

Table 1: Properties of the riser model

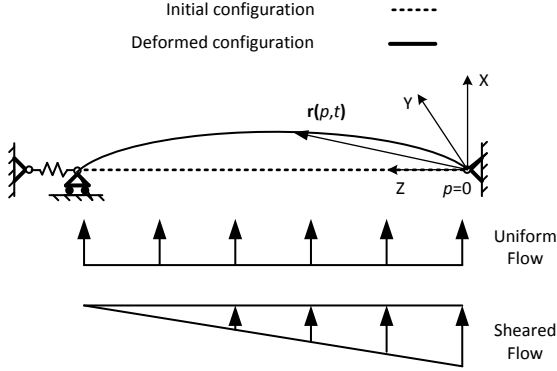| Parameters	Values	Dimension
External diameter	0.03	m
Length	38	m
Aspect ratio	1266	-
Bending Stiffness	572.3	Nm^2
Axial Stiffness	7.82×10^6	N
Mass	1.088	kg/m
Mass ratio	1.54	-

Fig. 2: Configuration of the riser and the coordinate system .

MARINTEK Offshore Basin Laboratory [16]. In the experiments, a riser of 38 meters is dragged horizontally or rotated around one end through still water to simulate a uniform and linearly sheared current. The key properties of the riser are presented in Table 1. The configuration of the riser, as well as the definition of the coordinate system, is illustrated in Fig.2. An initial tension of 6 kN is applied and one end of the riser is attached to a spring, while the other is pinned. The reason for using a spring is to simulate the restoring force provided by the pendulum with heavy clamp weight in the experiments. Without knowing the exact stiffness that the pendulum provides, the stiffness of the spring in the simulation is set to be 5×10^4 N/m.

The riser is simplified into a beam. In line with the Euler-Bernoulli beam theory, only the axial and bending deformations are considered. The configuration of the structure is described by the position vector $\mathbf{r}(p, t)$ of the cylinder axis as

$$\mathbf{r}(p, t) = \begin{bmatrix} x(p, t) \\ y(p, t) \\ z(p, t) \end{bmatrix} \tag{8}$$

where p is the Lagrange coordinate or arc-length measured along the undeformed cylinder, and t is the time. For the convenience of writing, the following notation

will be used to represent the partial derivative with respect to p: $\mathbf{r}_{,p} = \partial \mathbf{r}/\partial p$ and overdots represent the derivative with respect to time.

The weak forms of the equations of motion is given as

$$\delta W_I + \delta W_S - \delta W_E = 0 \tag{9}$$

where δW_I denotes the virtual work of inertia forces, δW_S is the virtual work of internal (elastic) forces, and δW_E is the virtual work of external forces.

The expressions of δW_I and δW_S are given as

$$\delta W_I = \int_0^L m_0 \ddot{\mathbf{r}}^T \delta \mathbf{r} dp \tag{10}$$

$$\delta W_S = \int_0^L \left(EA\epsilon_0 \delta\epsilon_0 + EIK\delta K \right) dp \tag{11}$$

where L is the length of undeformed beam, m_0 is the mass of the beam per unit length, E is the modulus of elasticity, A is the cross-sectional area and I is the second moment of the area. Furthermore, ϵ_0 is the axial strain, which is defined as

$$\epsilon_0 = |\mathbf{r}_{,p}| - 1 \tag{12}$$

and K, interpreted in [17] as the *material measure of curvature*, is defined as

$$K = \frac{|\mathbf{r}_{,p} \times \mathbf{r}_{,pp}|}{|\mathbf{r}_{,p}|^2} \tag{13}$$

The wake oscillators, presented in Section 2.1, are uniformly distributed along the riser to simulate the hydrodynamic force acting on it. Then, the coupled system is solved numerically using finite element method with Hermite shape functions; for detailed descriptions of the model please refer to Part I (submitted).

3 Response of the structure

In this section, the simulated responses of the riser subjected to uniform and linearly sheared flows are analysed. Simulations have been conducted at several flow velocities. Typical responses at two flow velocities $V = 0.5$ m/s and 1.5 m/s for the uniform flow, as well as at $V = 1.5$ m/s and 2.5 m/s for the linearly sheared flow, are presented. For the linearly sheared flow profile, the notation V represents the maximum flow velocity at $p = 0$.

3.1 Uniform flow

In this subsection, the simulated VIV of the riser subjected to uniform flow is discussed. The structural response patterns are quantified and analysed in the wavenumber-frequency domain after performing a spatial-temporal spectral analysis based on the 2D Fourier transform, and the complex modes at dominant frequencies are extracted.

Flow velocity at $V = 0.5$ m/s

The simulation results of the response of the riser subjected to a uniform flow at $V = 0.5$ m/s are depicted in Fig.3 and Fig.4, where the 2D PSD of nondimensional displacements and the corresponding complex modes at dominant frequencies are presented for all three models. For Model A, the 2D PSD of nondimensional cross-flow and in-line displacements, as illustrated in Figs.3(a) and (b), indicate that the structural response is at a single frequency in both directions. The dominant in-line response frequency, indicated by arrows in Fig.3(b), is $f_x \approx 1.632f_s$, which is approximately twice that of the cross-flow response $f_y \approx 0.816f_s$. In Figs.3(a) and (b), it is difficult to determine the wavenumber at which the riser is excited, since the energy seems to spread over a wide range of wavenumbers. This is because the FFT in the spatial domain suffers from a small number of spatial cycles. By observing the complex modes extracted at the dominant frequencies, it is deduced that the wavenumbers corresponding to the 3rd and 6th modes are excited in cross-flow and in-line directions respectively. The natural frequencies of the corresponding free vibration modes are indicated in Figs. 3(a) and (b) by red crosses; those natural frequencies are slightly smaller than the actual vibration frequencies in both the cross-flow and in-line directions. In Figs.4(a) and (b), the spanwise evolution of the amplitudes and phases of the complex modes extracted at dominant frequencies of structural responses in both cross-flow and in-line directions is presented. The cross-flow vibrations predicted by Model A are clearly in the form of standing waves, as definite nodes and jumps of π in the phase are observed in Fig.4(a). The maximum cross-flow vibrations are observed at the antinodes, which are as high as $1.4D$. In the in-line direction, see Fig.4(b), the structural response exhibits a mixed standing-travelling character. The evolution of the magnitude and phase of the complex mode suggests that the in-line vibration is excited at the middle of the riser and propagates towards both ends, developing strong standing waves near boundaries. The maximum in-line vibration, around $0.3D$, is

observed at the anti-nodes of the standing wave near boundaries.

In Fig.3(c,d) and Fig.4(c,d), the simulated riser responses are illustrated for Model B. As can be seen in Figs.3(c) and (d), Model B predicts the riser to vibrate at higher wavenumbers (corresponding to the 4th mode in the cross-flow direction and the 8th mode in the in-line direction) and higher frequencies ($f_y \approx 1.029f_s$ and $f_x \approx 2.058f_s$) compared to those of Model A. The simulated cross-flow vibrations are in good agreement with the free vibration structural modes regarding the excited wavenumber and frequency, while slight deviations are observed in the in-line response where the actual vibration frequency is lower than the corresponding natural frequency. The complex modes at the dominant frequencies, as depicted in Figs.4(c) and (d), indicate that the cross-flow vibration is dominated by a standing wave, while a predominant travelling wave is observed in the in-line direction. Although the evolution of the amplitude of the in-line complex mode suggests the same response pattern as that predicted by Model A, the evolution of the phase along the span displays unclear variation patterns. Such variations in the phase along the span were found to be associated with the fact that two different wavenumbers are excited in the in-line direction at the same frequency due to the unconstrained boundary in the Z direction at one end of the riser. Concerning the maximum magnitude of vibration, Model B predicts that the maximum cross-flow and in-line amplitudes of vibration are $0.8D$ and $0.15D$; both are smaller than those of Model A.

The simulation results of Model C, as pictured in Fig.3(e,f) and Fig.4(e,f), are similar to those of Model B; therefore, they are not discussed in detail here. However, it needs to be noted that while Model C predicts the same level of cross-flow vibration as Model B, it predicts the maximum in-line vibration around $0.075D$, which is much smaller than that simulated by the other two models.

Flow velocity at $V = 1.5$ m/s

For the case of $V = 1.5$ m/s, the 2D PSD of nondimensional cross-flow and in-line displacements and the corresponding dominant complex modes are presented in Fig.5(a,b) and Fig.6(a,b), respectively, for Model A. The predominant wavenumbers corresponding to the 8th and 16th modes are excited in the cross-flow and in-line directions at frequencies of $f_y \approx 0.914f_s$ and $f_x \approx 1.828f_s$ respectively. In both directions, the actual vibration frequencies are higher than the natural frequencies of the corresponding modes. The different positive and negative wavenumber peaks for the same frequency imply that the structural response is charac-

Fig. 3: Spatio-temporal spectra of (a,c,e) cross-flow and (b,d,f) in-line displacements at uniform flow $V = 0.5$ m/s using Model A (a,b); Model B (c,d) and Model C (e,f). The arrows represent the dominant frequencies. The wavenumbers and natural frequencies of selected free vibration modes are indicated by black vertical dashed lines and red crosses respectively.
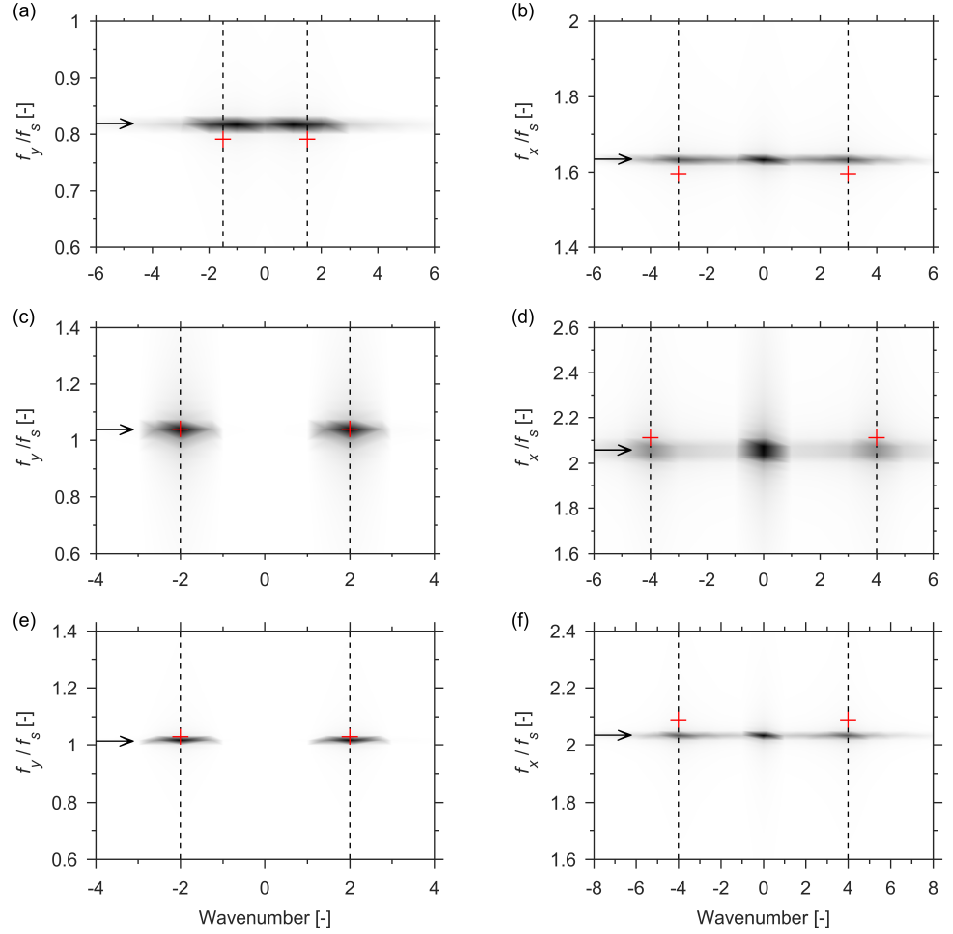
terised by mixed standing-travelling waves. The mixed standing-travelling character of the structural response is confirmed by the spanwise evolution of the amplitude and phase of the cross-flow and in-line complex modes; see Figs.6(a) and (b). The generally decreasing trend of the phase denotes the travelling wave oriented from $p/L = 0$ towards $p/L = 1$. In the case of a pure travelling wave, the variation of the phase is strictly linear. The modulation of the underlying standing character of the structural response leads to a zigzagging evolution pattern of the phase in both the cross-flow and in-line directions. From this point of view, the travelling wave is more predominant in the in-line response, as the evolution of the phase of the in-line complex mode is less modulated. The evolution of the magnitudes along the span reveals that both cross-flow and in-line displacements gradually increase along the direction of the travelling wave and reach their maximum – around $1.7D$ in the cross-flow direction and $0.3D$ in the in-line direction – at the end of the riser where standing waves dominate. This may imply that the energy is continually transferred from the fluid to the riser as the travelling wave propagates. It is also interesting to notice

from Fig.6(b) that the standing character of the in-line displacement seem to be associated with the cross-flow response. The ripples of the magnitude of the in-line complex mode, as a result of the modulation of the standing wave, display a pattern of a mixture of large cells that are consistent with the cross-flow response and small ripples. This is a result of the nonlinear coupling effect between the cross-flow and in-line motions which can only be captured by a nonlinear structural model.

Predictions by Models B and C are similar, as can be seen in Fig.5(c-f) and Fig.6(c-f). Both models predict that wavenumbers corresponding to the 9th and 18th modes will be excited in the cross-flow and in-line directions respectively. However, the cross-flow and in-line dominant frequencies predicted by Model B are $f_y \approx 1.055 f_s$ and $f_x \approx 2.110 f_s$ respectively, which are higher than those predicted by Model C ($f_y \approx 0.992 f_s$ and $f_x \approx 1.984 f_s$). The reason for such a difference is related to the tension increase due to the amplification of in-line forces. Model C, as will be demonstrated in Section 5, underestimates the amplification of the in-line force and therefore predicts a smaller tension
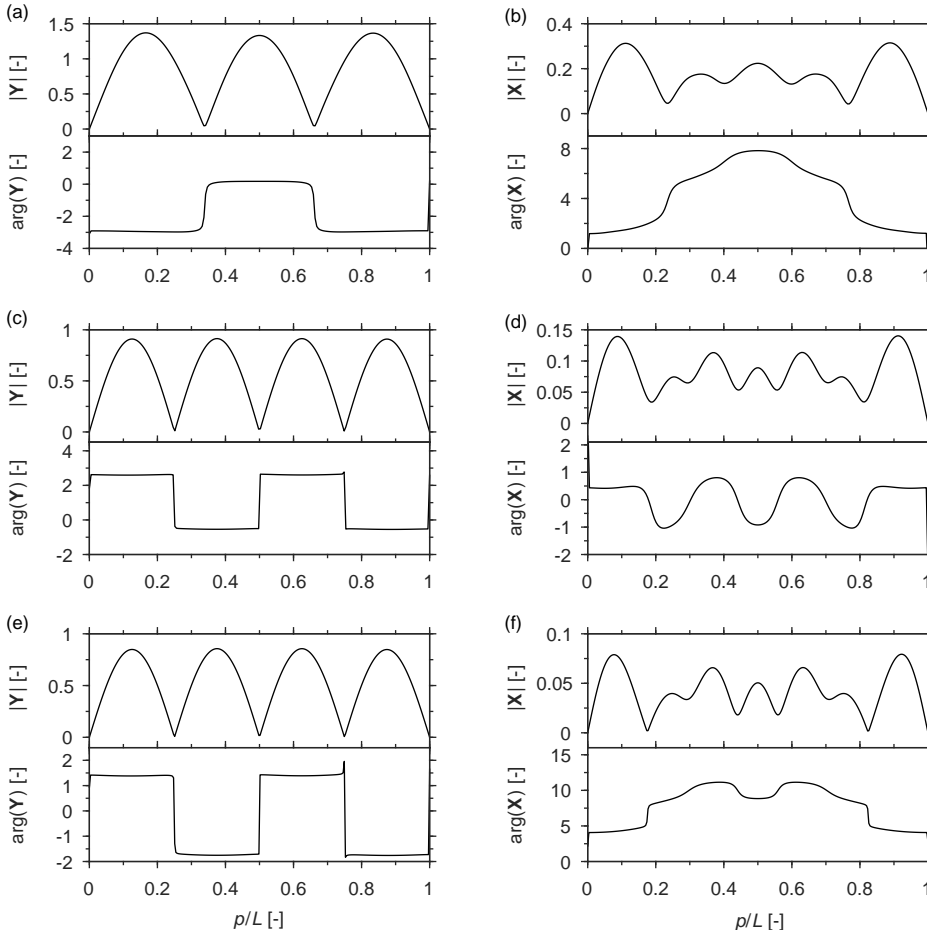
Fig. 4: Amplitude and phase of (a,c,e) cross-flow and (b,d,f) in-line complex modes at uniform flow $V = 0.5$ m/s. (a,b) correspond to the response obtained using Model A; (c,d) correspond to the response obtained using Model B and (e,f) correspond to the response obtained using Model C. The complex modes are extracted at dominant frequencies identified from Spatio-temporal spectra.

compared to Model B. As a result, the lock-in at the same mode for the two cases corresponds to different natural frequencies, as indicated by crosses in Figs.5(c) and (e). The dominant frequencies are in good agreement with the corresponding natural frequencies in the cross-flow direction but are higher than natural frequencies in the in-line direction for both models. The cross-flow complex modes at dominant frequencies indicate that for both models, the cross-flow vibration exhibits a standing-travelling character; however, different from Model A, the vibration is dominated by standing waves. The underlying travelling wave pattern for both Models can be observed by the general increasing trend of the phase along the span, indicating that the direction of the travelling wave is opposite to that of Model A. The maximum cross-flow vibration of Model B is around $1.0D$, which is similar to the prediction of Model C, while the predicted maximum in-line vibration of Model B is around $0.13D$, which is slightly larger than the prediction of Model C around $0.1D$.

3.2 Linearly sheared flow

In this subsection, the simulated VIV of the riser subjected to linearly sheared flow are presented. The flow profile is such that the velocity at $p/L = 1$ is zero and that at $p/L = 0$ is maximum. The notation V denotes the maximum flow velocity throughout this subsection.

Flow velocity at $V = 1.5$ m/s

In Fig.7 the 2D PSD of non-dimensional cross-flow and in-line displacements are presented for all three models. In all plots, the vibration frequencies are normalised by the Strouhal frequency that was calculated at the maximum flow velocity. As can be seen from Fig.7, all three models predict a single frequency response in both the cross-flow and in-line directions, and the in-line dominant frequencies are approximately twice those of the cross-flow responses. A comparison of the results reveals that the models without an in-line coupling term in the wake oscillator equation (Models B and C) predict similar responses to the model with in-line coupling (Model A) regarding the excited wavenumber and dominant frequency. In general,

Fig. 5: Spatio-temporal spectra of (a,c,e) cross-flow and (b,d,f) in-line displacements at uniform flow $V = 1.5$ m/s using Model A (a,b); Model B (c,d) and Model C (e,f). The arrows represent the dominant frequencies. The wavenumbers and natural frequencies of selected free vibration modes are indicated by black vertical dashed lines and red crosses respectively.
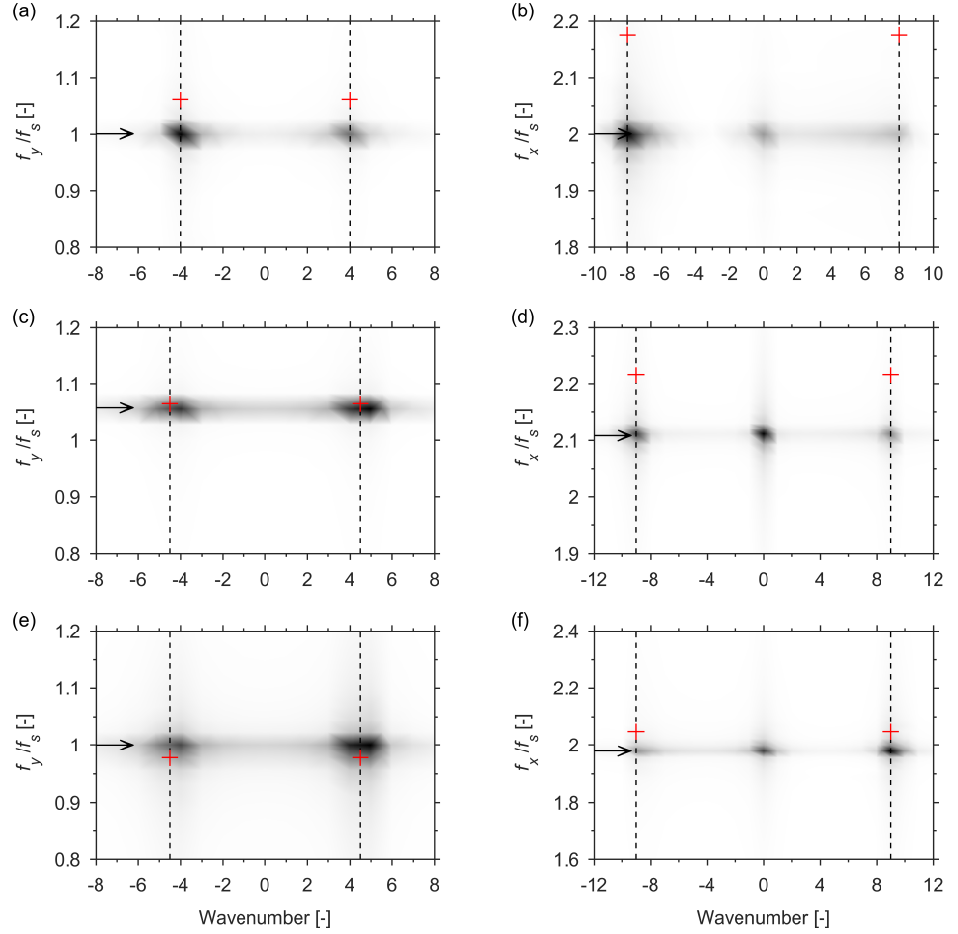
Model A predicts that the riser will vibrate at slightly higher frequencies ($f_y \approx 0.933f_s$ and $f_x \approx 1.867f_s$) compared to those of Model B ($f_y \approx 0.904f_s$ and $f_x \approx 1.807f_s$) and Model C ($f_y \approx 0.891f_s$ and $f_x \approx 1.782f_s$). For all three models, the wavenumber corresponding to the 10th mode is excited in the cross-flow direction; moreover, according to Models A and C, the in-line wavenumber corresponding to the 20th mode is excited, whereas Model B predicts that the in-line wavenumber corresponding to the 22th mode is excited. The perceptibly larger negative wavenumber peaks compared to the positive ones imply that the travelling waves are predominant in the structural responses for all three models in both the cross-flow and in-line directions, and these waves propagate from the high-velocity region (near $p/L = 0$) towards the low-velocity region (near $p/L = 1$).

The travelling-wave-dominant structural responses of all three models are confirmed by the complex modes at the dominant frequency, as illustrated in Fig.8. In the cross-flow direction, the maximum amplitude of the structural complex mode of Model A is observed around $p/L = 0.45$ and exceeds $0.4D$, while that of Models B

and C occurs at $p/L = 0.28$ and is close to $0.3D$. Concerning the in-line vibration, Model A predicts the highest amplitude of vibration around $0.075D$, followed by Model B, with a maximum around $0.045D$, and Model C predicts the smallest maximum amplitude, which is smaller than $0.02D$.

Flow velocity at $V = 2.5$ m/s

The simulated VIV of the riser subjected to a sheared flow velocity with maximum velocity $V = 2.5$ m/s are presented in Fig.9, Fig.10 and Fig.11. In Fig.9, the 2D PSD exhibits a multiple frequency response in both the cross-flow and in-line directions for all three models. Although several frequencies are excited in the cross-flow response, only the first two dominant frequencies that contain the most energy are considered; they are indicated by arrows in Figs.9(a), (c) and (e). Here, the strongest frequency is denoted as the main dominant frequency and the other one as the secondary dominant frequency. For the in-line response, a substantial amount of energy concentrates at low frequencies; the reason for this has been explained in Part I (submitted), which is the result of a slowly varying component
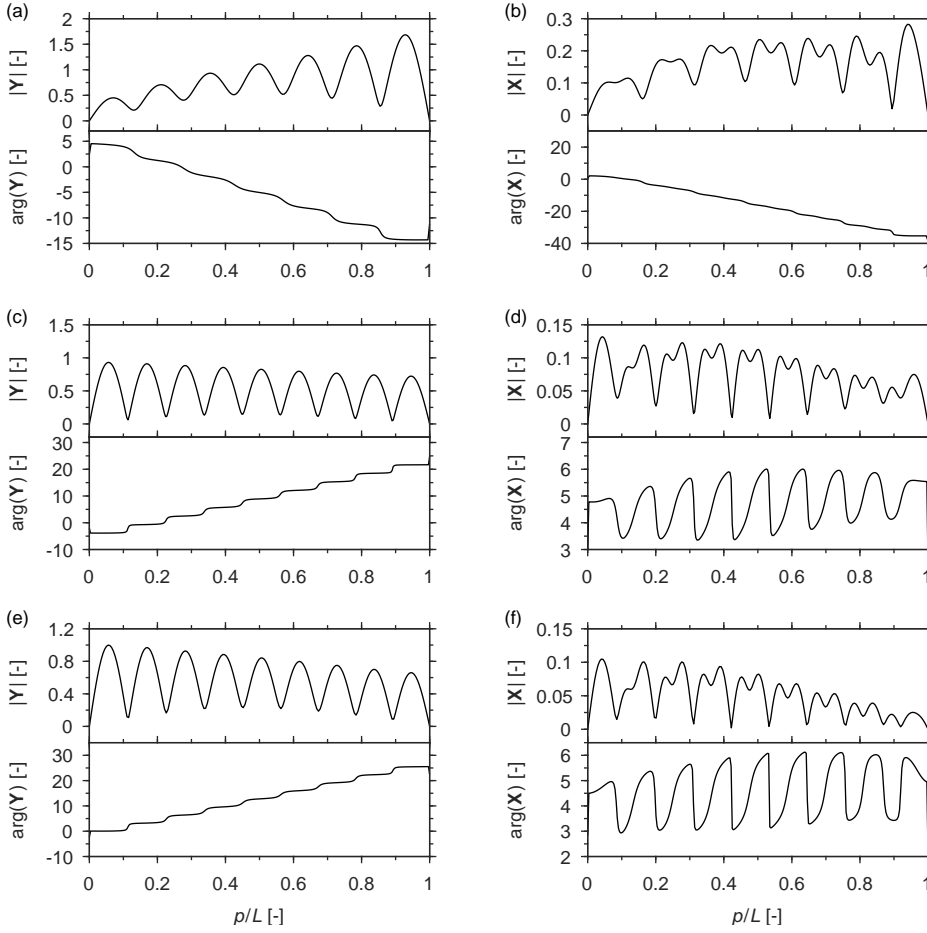
Fig. 6: Amplitude and phase of (a,c,e) cross-flow and (b,d,f) in-line complex modes at uniform flow $V = 1.5$ m/s. (a,b) correspond to the response obtained using Model A; (c,d) correspond to the response obtained using Model B and (e,f) correspond to the response obtained using Model C. The complex modes are extracted at dominant frequencies identified from Spatio-temporal spectra.

in the in-line force caused by the modulated cross-flow motion. Apart from this component at low frequencies, the excited frequencies that are close to twice those of the dominant cross-flow frequencies are chosen as the dominant in-line frequencies, indicated by arrows in Figs.9(b), (d) and (f). At each dominant frequency, the corresponding excited wavenumber and natural frequency are also presented. For Model A, the main dominant cross-flow frequency is $f_y \approx 0.914 f_s$, with an excited wavenumber corresponding to the 13th mode. Models B and C, on the other hand, predict dominant frequencies $f_y \approx 0.904 f_s$ and $f_y \approx 0.871 f_s$ respectively, with excited wavenumbers that correspond to the 14th mode for both cases. Concerning the secondary dominant cross-flow frequency, all three models predict it to be around $f_y \approx 0.3 f_s$, with an excited wavenumber corresponding to the 4th mode. In the in-line direction, the main dominant frequencies are $f_y \approx 1.838 f_s$, $f_y \approx 1.806 f_s$ and $f_y \approx 1.743 f_s$ for Models A, B and C respectively, and the corresponding excited wavenumbers are at the 26th, 30th and 29th modes. Similar to the cross-flow case, all three models predict the same secondary dominant in-line frequency around

$f_y \approx 0.6 f_s$, with a wavenumber that corresponds to the 8th mode.

The complex modes at the main and secondary dominant frequencies are presented in Fig.10 and Fig.11 in both the cross-flow and in-line directions. As can be seen from Fig.10, at the main dominant frequencies, both cross-flow and in-line vibrations are associated with travelling waves that propagate from the high-velocity region towards the low-velocity region. All three models predict similar maximum cross-flow vibrations – close to $0.4D$ – at the main dominant frequency, while Model A predicts the largest in-line vibration with a maximum value around $0.1D$, followed by Model B around $0.05D$ and Model C around $0.02D$. For the complex modes at the secondary dominant frequency, as illustrated in Fig.11, all three models predict similar cross-flow vibrations, which are in the form of decaying travelling waves propagating towards the high-velocity region over a span between $p/L = 0$ and 0.7 and are dominated by standing waves near $p/L = 1$. This implies that the vibrations at the secondary dominant frequency are excited around $p/L = 0.7$ and propagate towards both ends of the riser. Models B and C predict

Fig. 7: Spatio-temporal spectra of (a,c,e) cross-flow and (b,d,f) in-line displacements at sheared flow $V = 1.5$ m/s using Model A (a,b), Model B (c,d) and Model C (e,f). The arrows represent the dominant frequencies. The wavenumbers and natural frequencies of selected free vibration modes are indicated by black vertical dashed lines and red crosses respectively.
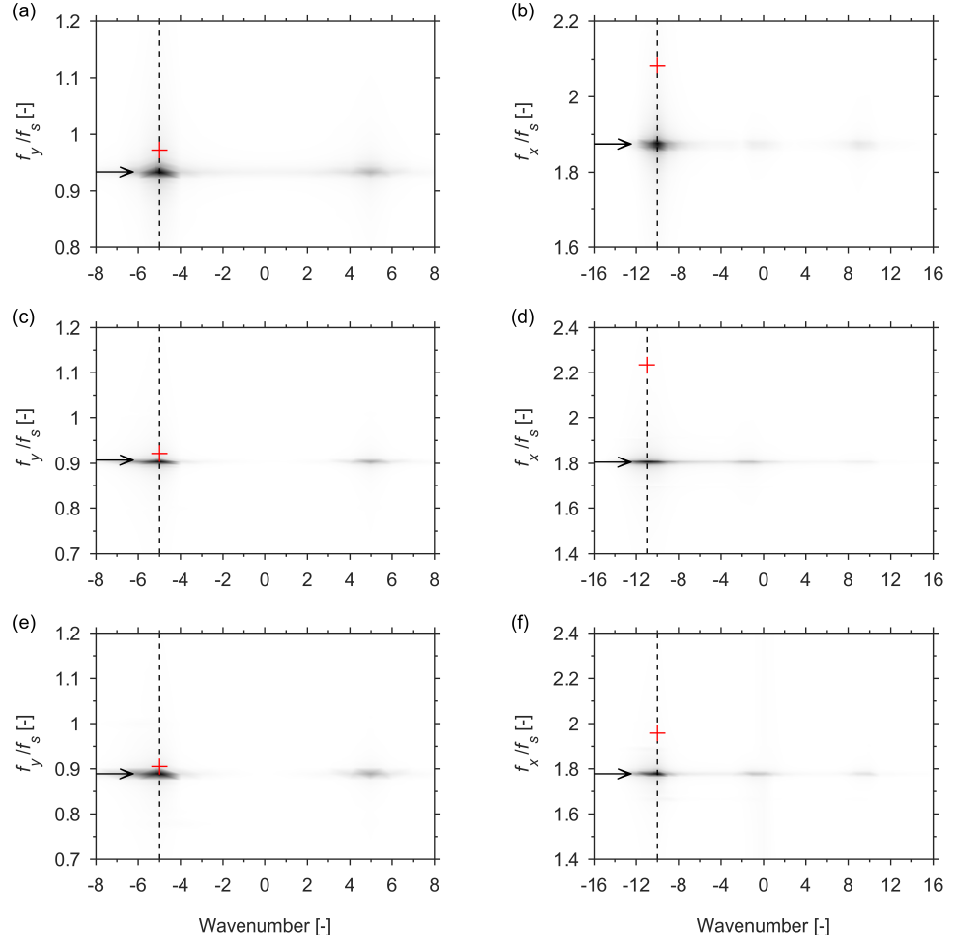
a similar maximum cross-flow vibration around $0.13D$, which is slightly smaller than the prediction of Model A that is close to $0.16D$. Concerning the in-line vibration at the secondary dominant frequency, see Figs.11(b), (d) and (f), the pattern of the magnitude of complex modes are similar for all three cases; however, the evolutions of the phase are different. All three models predict that the in-line vibration at the secondary dominant frequency will mainly occur between $p/L = 0.7$ and 1 and will be standing wave dominated. Model A predicts the largest vibration magnitude with a maximum value close to $0.08D$, whereas Models B and C predict smaller values around $0.04D$ and $0.02D$ respectively. For the rest of the span, from $p/L = 0$ to $p/L = 0.7$, the amplitudes of the in-line vibrations are small. Over the span $p/L = 0-0.7$, the almost linearly decreasing phase shown in Fig.11(b) indicates that Model A predicts the vibration in the form of a travelling wave that travells towards the low-velocity region. Model B, on the other hand, predicts that a large segment of the riser is associated with a travelling wave that propagates towards the high-velocity region, as indicated in Fig.11(d) where the phase increases over $p/L = 0.2-0.6$. In Fig.11(f), it

can be seen that the phase of the in-line complex mode remains almost constant over $p/L = 0-0.7$, according to Model C.

4 Phase difference between cross-flow and in-line motions

The phase difference between the cross-flow and in-line motions has a significant influence on the wake pattern when VIV occurs. It affects the hydrodynamic force acting on the structure and consequently influences the energy transfer between the fluid and structure. As a result, in VIVs of flexible cylinders, the phase difference is naturally related to the distribution of excitation and damping regions. In this section, the definition of the phase difference, as well as the corresponding trajectory of structural motion, is presented in subsection 4.1. The phase differences for all simulation cases are calculated and discussed in subsection 4.2.
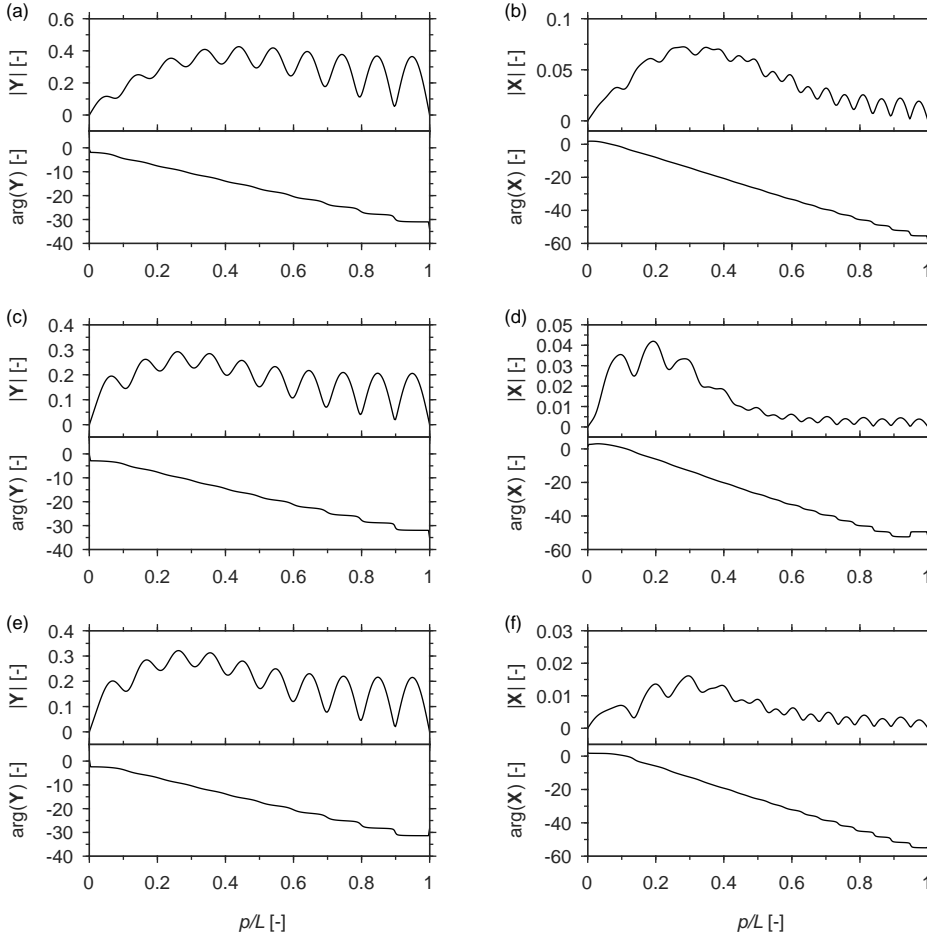
Fig. 8: Amplitude and phase of (a,c,e) cross-flow and (b,d,f) in-line complex modes at s-heared flow $V = 1.5$ m/s. (a,b) correspond to the response obtained using Model A; (c,d) correspond to the response obtained using Model B and (e,f) correspond to the response obtained using Model C. The complex modes are extracted at dominant frequencies identified from Spatio-temporal spectra.

4.1 Definition of phase difference and motion trajectory

Assume that the motion of a cross-section of the riser in the cross-flow and in-line directions can be described by the following equations:

$$y = y_0 \cos\left(\omega t + \phi_y\right) \tag{14}$$

$$x = x_0 \cos\left(2\omega t + \phi_x\right). \tag{15}$$

Then, the phase difference is defined as $\phi_{xy} = \phi_x - 2\phi_y$. This definition is in accordance with [7] but has a shift of 90° compared to the one given by [1]. With such a definition, the values of ϕ_{xy} in the range of 0°−180° correspond to a counter-clockwise motion trajectory, and those in the range of 180°−360° correspond to a clockwise orbit. Here, the counter-clockwise motion corresponds to the trajectory where the cylinder moves a-gainst undisturbed flow when reaching the cross-flow oscillation maximum, while the clockwise motion is associated with the case where the cylinder moves in the opposite direction. The in-line and cross-flow phases

ϕ_x and ϕ_y can be obtained by the angle of the complex modes determined in the previous section as $\phi_x = \arg(\mathbf{X})$ and $\phi_y = \arg(\mathbf{Y})$.

It must be clarified that the concept of phase d-ifference and the application of $\phi_{xy} = \phi_x - 2\phi_y$ on-ly make sense when the cross-flow and in-line motions are synchronised. Here, synchronisation means that the cross-flow and in-line motions vibrate interdependently at a constant frequency ratio of 2. In the experiments, this is not always the case, as the noise can sometimes be strong [18]. However, this is not a problem here, as the simulation results indicate good synchronisation between the cross-flow and in-line motions along the whole span for all simulated cases. Some examples of such synchronisation and values of ϕ_{xy} that are spec-ified for different motion trajectories are presented in Fig.12 for Model A.

4.2 Discussion

The phase difference ϕ_{xy} is calculated for all simulation results. The distributions of ϕ_{xy} along the riser are pre-

Fig. 9: Spatio-temporal spectra of (a,c,e) cross-flow and (b,d,f) in-line displacements at sheared flow $V = 2.5$ m/s using Model A (a,b), Model B (c,d) and Model C (e,f). The arrows represent the dominant frequencies. The wavenumbers and natural frequencies of selected free vibration modes are indicated by black vertical dashed lines and red crosses respectively.
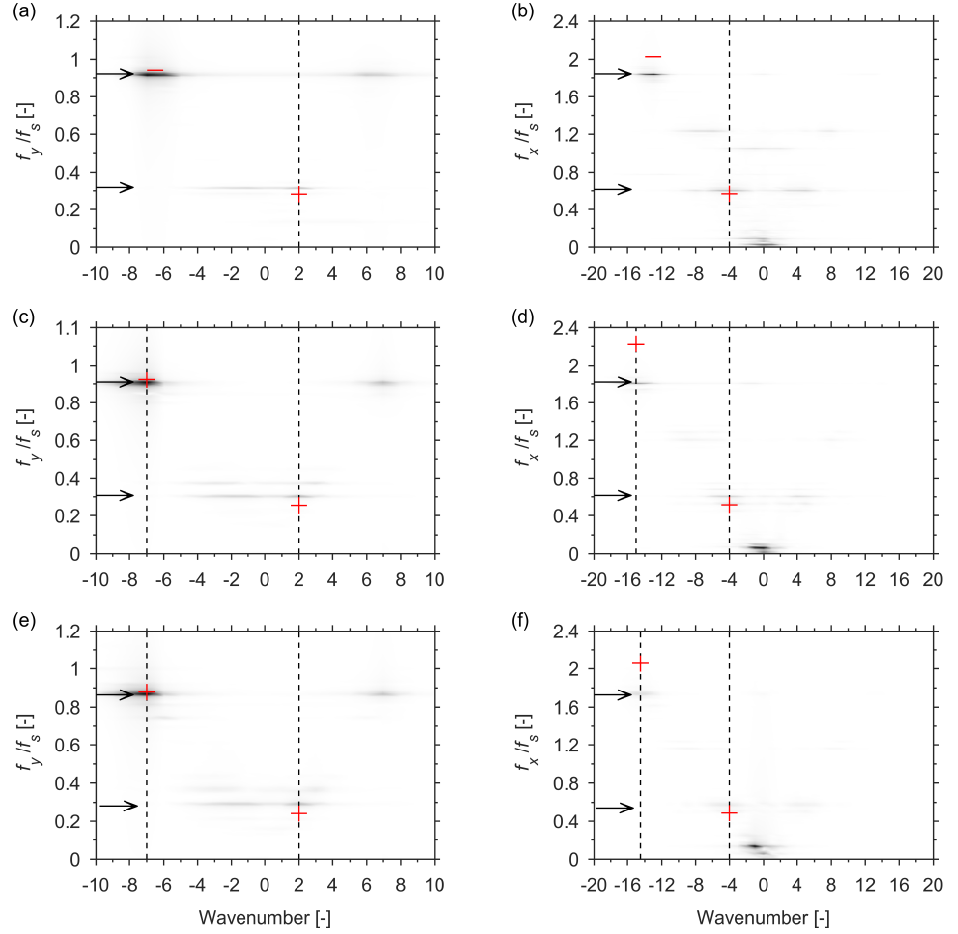
sented in Fig.13 and Fig.14 for the uniform flow cases and in Fig.15 for the sheared flow case. The boundary between the counter-clockwise and clockwise trajectory (180°) is indicated by a vertical thick line.

For the uniform flow case at $V = 0.5$ m/s, as illustrated in Fig.13, three models predict different distributions of ϕ_{xy} along the riser. For Model A, the phase difference along the riser covers a wide range of values between 0° and 360°, as can be seen in Fig.13(a). Jumps of approximately 310° occur at locations of $p/L = 0.64$ and $p/L = 0.36$, which are close to the locations of nodes between the cells of the cross-flow standing wave. The phase difference predicted by Model B, see Fig.13(b), varies around 0° and alternates between the counter-clockwise and clockwise regions. As depicted in Fig.4(d), the alternation is found to be closely related to the variation in the phase of the in-line motion, which, as explained in the previous section, is a result of the excitation of two different wavenumbers at the same frequency in the in-line direction. For Model C, the phase difference also varies between the counter-clockwise and clockwise regions, as pictured in Fig.13(c).

For the uniform flow case at $V = 1.5$ m/s, it is clear that the distribution of ϕ_{xy} for Model A, as portrayed in Fig.14(a), exhibits a different pattern compared to that of Models B and C, see Figs.14(b) and (c). For Model A, the mixed standing-travelling wave nature of both cross-flow and in-line displacements leads to a zigzagging evolution of ϕ_{xy} along the riser. The zigzagging pattern seems to be associated with the cells of the cross-flow displacement, if one compares Fig.14(a) with Fig.6(a), within which the phase difference continuously evolves to higher values at nodes and decreases through the cell before jumping again at the next node. The variation of ϕ_{xy} is smooth and confined mainly between 0° and 180°, corresponding to a counter-clockwise trajectory, except in the region near the upper boundary where the jumps of ϕ_{xy} at nodes exceed 180° as a result of dominant standing waves over that region in both the cross-flow and in-line directions. Concerning Models B and C, the evolution of ϕ_{xy} predicted by the two models is similar. As illustrated in Figs.14 (b) and (c), although ϕ_{xy} is mostly confined between 0° and 90°, significant segments of the span are associated with the ϕ_{xy} that sweeps through the range 180° − 360°.
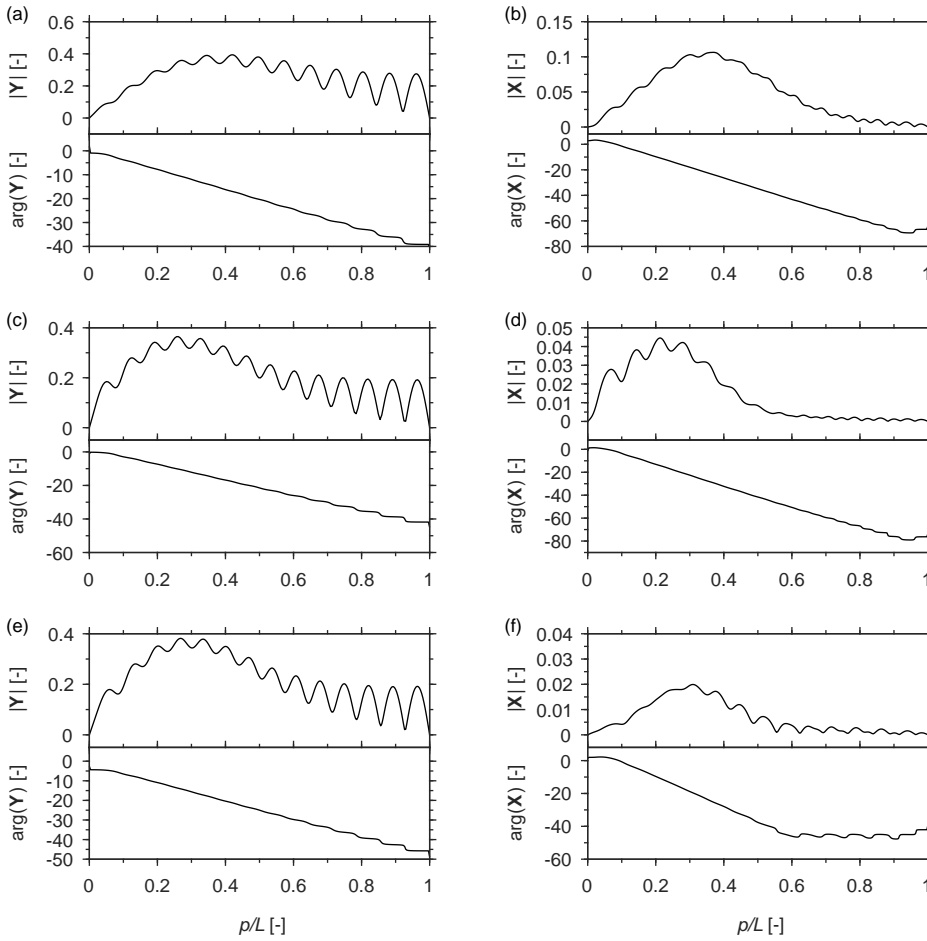
Fig. 10: Amplitude and phase of (a,c,e) cross-flow and (b,d,f) in-line complex modes at sheared flow $V = 2.5$ m/s for main dominant frequency. (a,b) correspond to the response obtained using Model A; (c,d) correspond to the response obtained using Model B and (e,f) correspond to the response obtained using Model C. The complex modes are extracted at main dominant frequencies identified from Spatio-temporal spectra.

The spanwise variation of the phase difference for the cases of sheared flow are presented in Fig.15. At flow velocity $V = 2.5$ m/s, the structural response contains multiple frequency components; therefore, only the results for the case of $V = 1.5$ m/s are presented here. Since the response patterns predicted by the three models are similar in sheared flow cases, it is expected that the distribution of the phase difference should also not be vastly different. The similarities between the predictions by the three models are obvious in Fig.15. For all three models, the phase differences are confined within the counter-clockwise region over a large segment of the riser near the high-velocity region as a result of a predominant travelling wave in both the cross-flow and in-line vibrations. The underlying standing character of the vibration leads to a zigzagging evolution of ϕ_{xy} along the span; this is similar to the case of uniform flow velocity $V = 1.5$ m/s in Model A. In the low-velocity region, close to the end of the riser where the standing wave becomes predominant, the variation of the phase difference becomes large and jumps to the clockwise region at some locations.

In general, if the distribution of the phase difference is compared with the corresponding response pattern, then when the travelling wave is predominant in the response (all the sheared flow cases and uniform flow cases of $V = 1.5$ m/s for Model A), the phase difference has a tendency to be confined within a counter-clockwise range. In contrast, when the standing wave dominates (all the uniform flow cases for Models B and C and the uniform flow case of $V = 0.5$ m/s for Model A), the phase difference alternatively switches between counter-clockwise and clockwise ranges. The observations made on the variation of the phase difference shown in this section will be correlated with the fluid-structure energy transfer in the next section.

5 Hydrodynamic forces and fluid-structure energy transfer

In this section, the hydrodynamic forces and the energy transfer between the structure and fluid are studied in relation to the structural responses analysed in Sections 3 and 4. The fluid forces, as well as the fluid-structure

Fig. 11: Amplitude and phase of (a,c,e) cross-flow and (b,d,f) in-line complex modes at sheared flow $V = 2.5$ m/s for secondary dominant frequency. (a,b) correspond to the response obtained using Model A; (c,d) correspond to the response obtained using Model B and (e,f) correspond to the response obtained using Model C. The complex modes are extracted at secondary dominant frequencies identified from Spatio-temporal spectra.
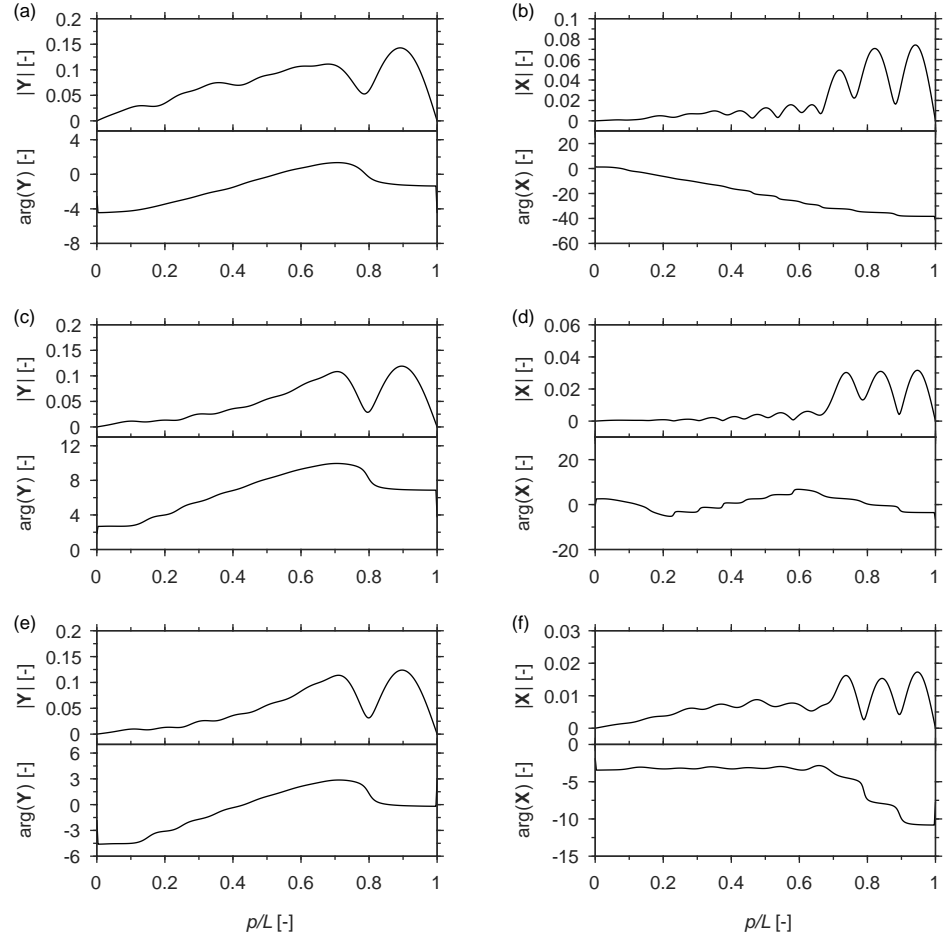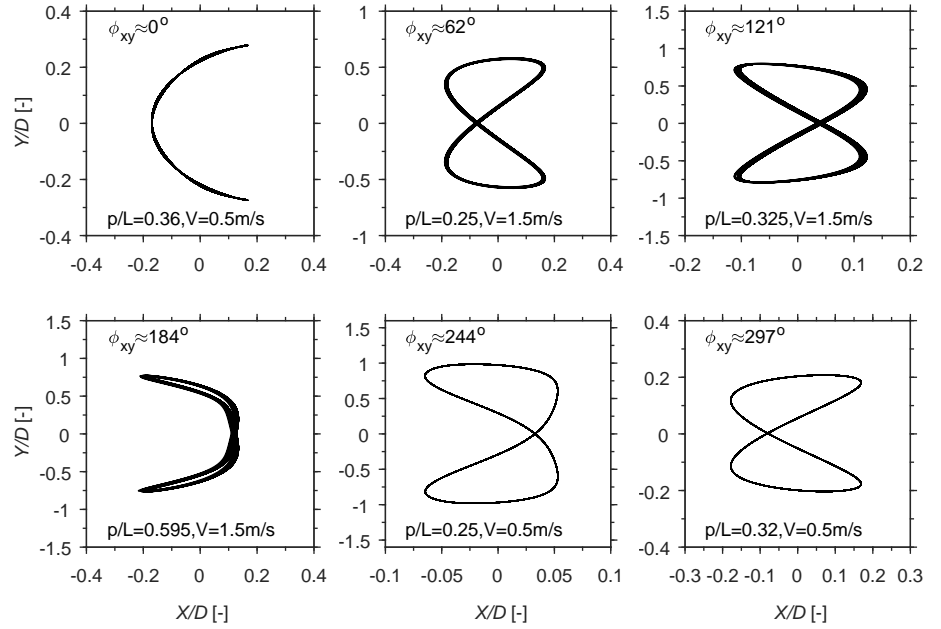

Fig. 12: Selected trajectories of the cylinder and corresponding phase difference from simulations with Model A.
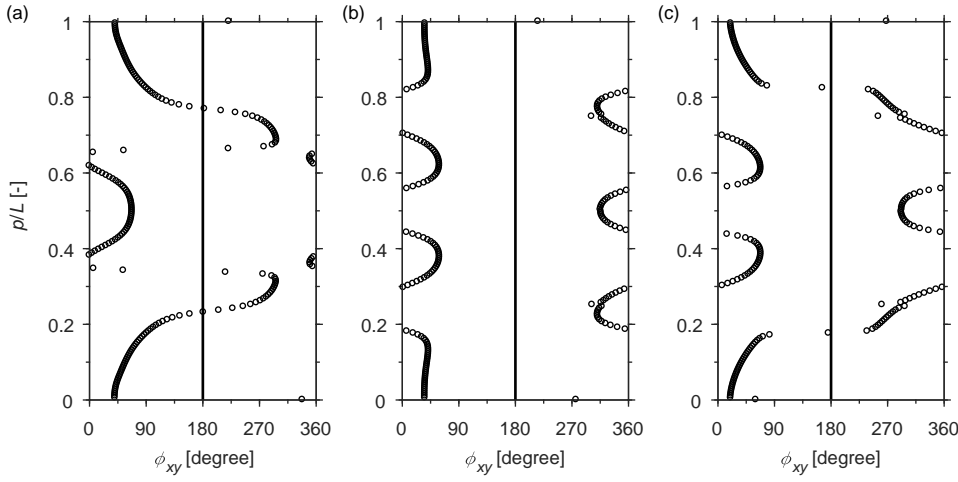
Fig. 13: Phase difference along the span at uniform flow $V = 0.5$ m/s for (a) Model A, (b) Model B and (c) Model C.
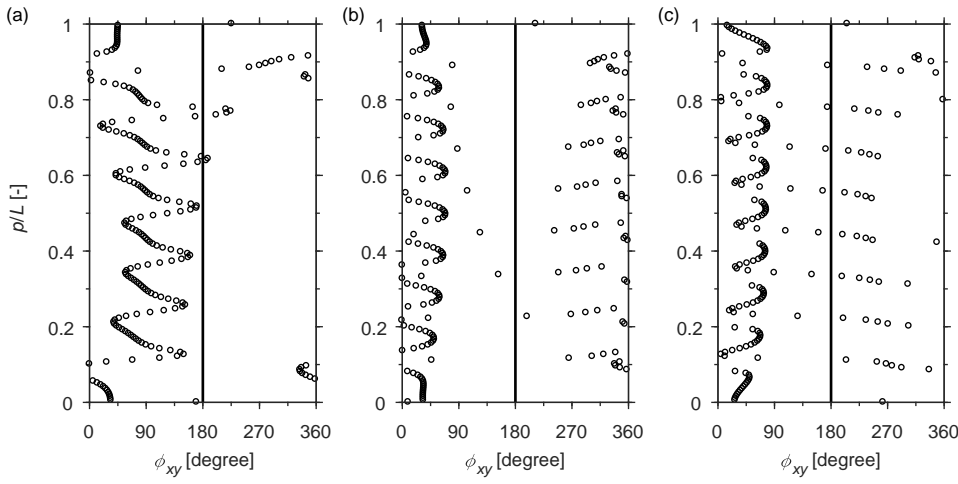
Fig. 14: Phase difference along the span at uniform flow $V = 1.5$ m/s for (a) Model A, (b) Model B and (c) Model C.
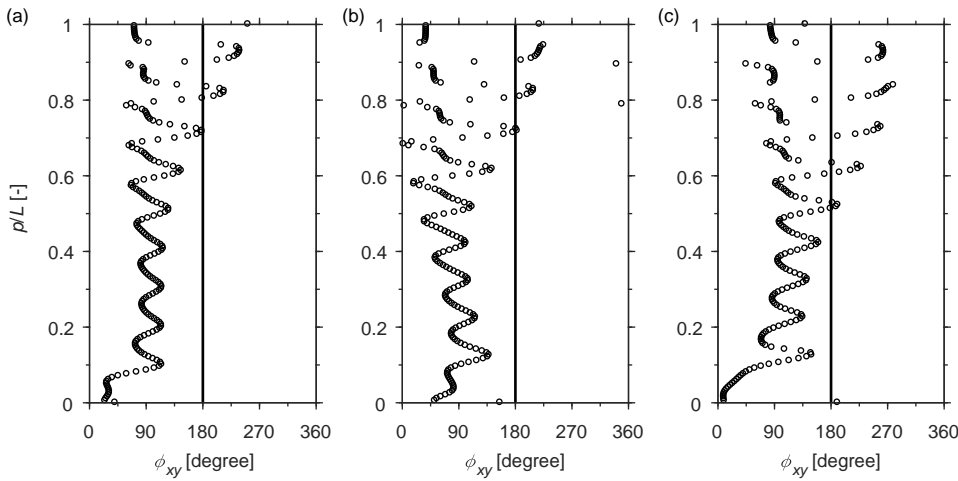
Fig. 15: Phase difference along the span at sheared flow $V = 1.5$ m/s for (a) Model A, (b) Model B and (c) Model C.

energy transfer, are representative of the nonlinear equilibrium state of the coupled fluid-structure system and decide the global structural behaviour. The prediction of the segments of the structure that the energy flows into (denoted as power-in region) and out from (denoted as power-out region) is of fundamental importance for VIVs of flexible structures.

5.1 Hydrodynamic forces

In this subsection, the hydrodynamic forces, as well as their distribution along the riser, are discussed based on the simulation results. The hydrodynamic forces exerted on the structure are calculated at each nodal location of the riser model from the simulated oscillations of wake variable q using Eqs.(29), (30) and (33) in Part I (submitted). It needs to be pointed out that the hydrodynamic force calculated here excludes the potential added mass. The calculated hydrodynamic force is a vector in the space, and only its components in cross-flow (F_y) and in-line (F_x) directions are considered. The cross-flow and in-line force coefficients, namely C_y and C_x, are obtained by normalising the corresponding forces using the following equation:

$$C_{x,y} = \frac{F_{x,y}}{\frac{1}{2}\rho D V^2}. \tag{16}$$

In Fig.16 and Fig.17, the RMS values of the mean in-line force coefficients, denoted as $\hat{C}_x$; the fluctuating in-line force coefficients, denoted as $\tilde{C}_x$; and the cross-flow force coefficients C_y are presented for all three models at uniform flow velocities of $V = 0.5$ m/s and $V = 1.5$ m/s. It is clear in Fig.16(a) and Fig.17(a) that all three models predict the amplification of $\hat{C}_x$ compared to its value, around 1.2, on a fixed cylinder, but at different levels. Model A predicts the most significant amplification of the mean in-line force coefficient and Model C predicts the least. From all three models, the amplification of the mean in-line force coefficient is found to be associated with large cross-flow vibrations of the riser. The maxima of $\hat{C}_x$ are located in the regions of antinodes of cross-flow motion. The same trend was reported in experiments by [19]. Furthermore, the magnitude of the simulated maximum mean in-line force coefficient by Model A – as high as 6 – is comparable to those observed in the experiments under a similar amplitude of cross-flow displacement. At the location where the cross-flow motion is close to zero, for example the cross-flow nodes at $V = 0.5$ m/s, the mean in-line force coefficient predicted by Model A is around 2, which is still higher compared to the case of a stationary cylinder, while the other two models predict almost no amplification.

The fluctuating component of the in-line force coefficients, as illustrated in Fig.16(b) and Fig. 17(b), has a similar trend to the mean in-line force. In general, the distribution of $\tilde{C}_x$ follows a shape similar to that of magnitude of cross-flow complex mode, meaning that it is still primarily affected by the cross-flow motion. In addition, the influence of the in-line motion is also significant, as the local maxima of fluctuating in-line forces appear mostly at points associated to the local maxima of the in-line displacements.

The distribution of the cross-flow force, in contrast to the in-line force, exhibits a more irregular pattern, as depicted in Fig.16(c) and Fig.17(c). The cross-flow forces predicted by Models B and C exhibit a similar pattern of distribution, with the magnitude calculated by Model B slightly higher than that by Model C. The cross-flow force obtained with Model A exhibits a different pattern. Also, Model A predicts, in general, a larger magnitude of cross-flow force. Efforts have been made to relate the variation of the cross-flow force to the structural motions. However, no obvious trend has been observed. This may imply that for all three models, the cross-flow force is sensitive to both the cross-flow and in-line motions. It is interesting to note that for the uniform flow case at $V = 0.5$ m/s where the cross-flow motion is dominated by standing waves, at the location where the cross-flow motion is almost zero, the cross-flow force predicted by Models B and C is close to zero, while that predicted by Model A still has a significant value.

The hydrodynamic forces for the sheared flow case with maximum flow velocity $V = 1.5$ m/s are presented in Fig.18. Different from the cases of uniform flow, the force coefficients are obtained by normalising the force with the maximum flow velocity. As a result, all the force coefficients exhibit a gradual decrease from the high-velocity region to the low-velocity region towards zero. The usage of the maximum flow velocity in the normalisation makes it difficult to make a direct comparison between the force coefficients and the response amplitude of the riser, as has been done for the uniform flow. However, by comparing the positions of the local maxima and minima, it is clear that the large mean and fluctuating in-line coefficients are normally found at locations of large cross-flow oscillation amplitude. With regard to the cross-flow force coefficient, its relation to the cross-flow amplitude is more complex. For example, in Fig.18(c), the local maxima of C_y are observed at the local minima of cross-flow vibration for $p/L < 0.5$, while for $p/L > 0.5$ the trend is the opposite.
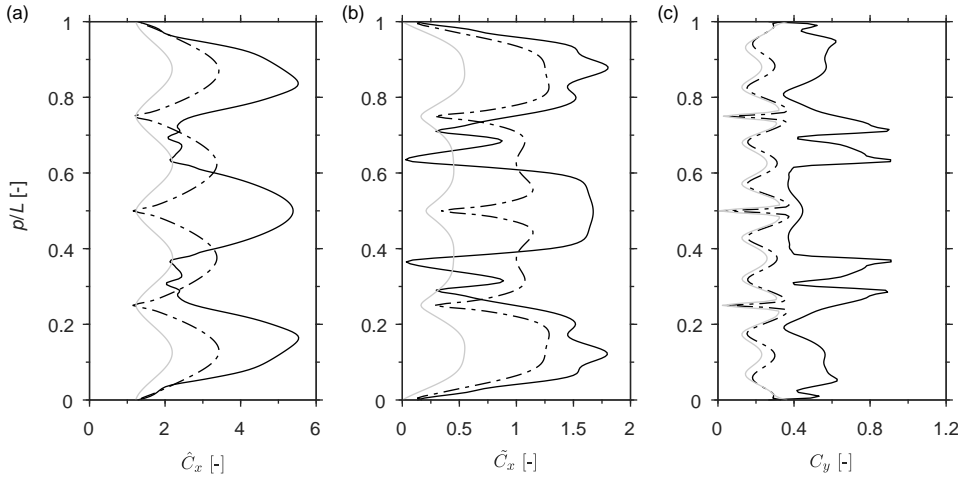
Fig. 16: RMS values of (a) mean in-line force coefficient $\hat{C}_x$, (b) fluctuating in-line force coefficient $\tilde{C}_x$ and (c) cross-flow force coefficient C_y for uniform flow velocity $V = 0.5$ m/s. Black solid lines represent results from Model A, black dashed lines represent results from Model B and grey solid lines represent results from Model C.
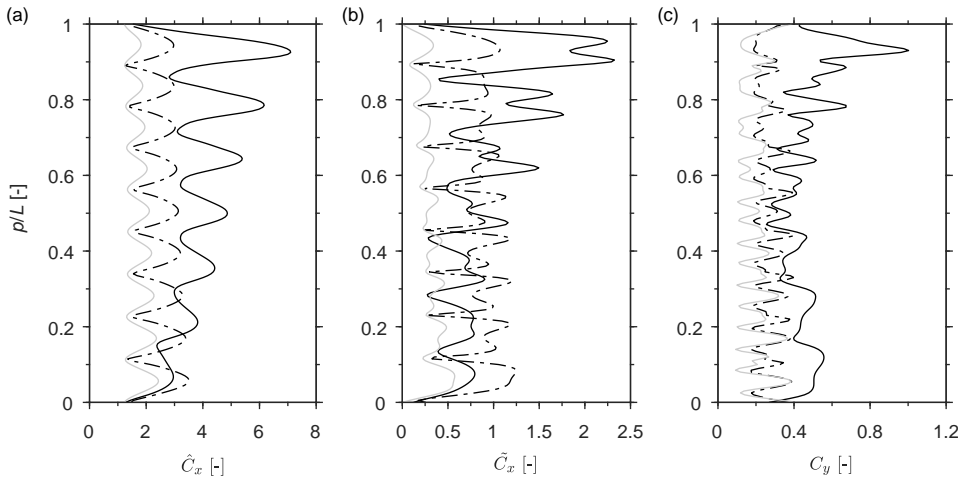
Fig. 17: RMS values of (a) mean in-line force coefficient $\hat{C}_x$, (b) fluctuating in-line force coefficient $\tilde{C}_x$ and (c) cross-flow force coefficient C_y for uniform flow velocity $V = 1.5$ m/s. Black solid lines represent results from Model A, black dashed lines represent results from Model B and grey solid lines represent results from Model C.
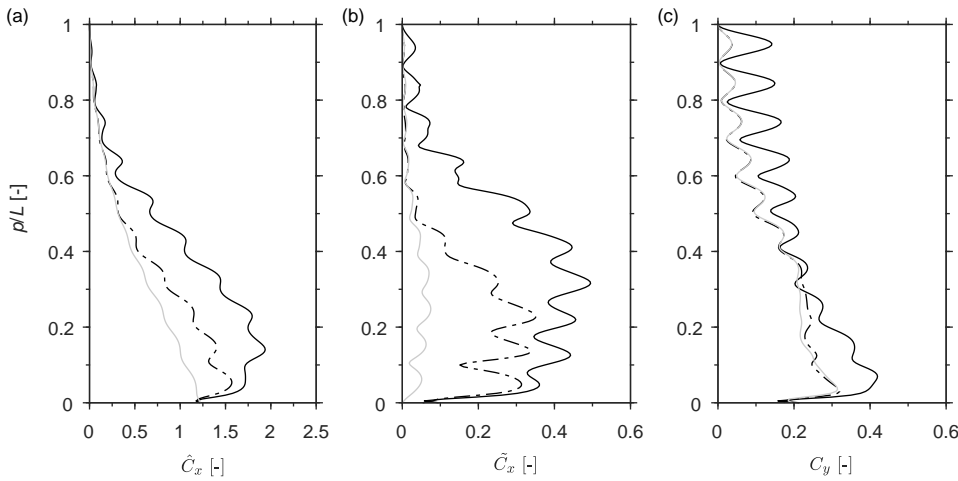
Fig. 18: RMS values of (a) mean in-line force coefficient $\hat{C}_x$, (b) fluctuating in-line force coefficient $\tilde{C}_x$ and (c) cross-flow force coefficient C_y for sheared flow with maximum velocity $V = 1.5$ m/s. Black solid lines represent results from Model A, black dashed lines represent results from Model B and grey solid lines represent results from Model C.

5.2 Fluid-structure energy transfer

Follow the concept used by [20], the energy transfer between the fluid and structure in this paper is quantified by the force coefficient that is in phase with the velocity of the riser; for simplicity, it is denoted as excitation coefficient C_e here. Its components in the cross-flow and in-line directions are defined as

$$C_{e,y} = \frac{\frac{2}{T}\int_T C_y \dot{y} dt}{\sqrt{\frac{2}{T}\int_T \dot{y}^2 dt}} \quad (17)$$

and

$$C_{e,x} = \frac{\frac{2}{T}\int_T C_x \dot{x} dt}{\sqrt{\frac{2}{T}\int_T \dot{x}^2 dt}}. \quad (18)$$

The total force in phase with the velocity vector is defined as

$$C_e = \frac{\frac{2}{T}\int_T (C_y \dot{y} + C_x \dot{x}) dt}{\sqrt{\frac{2}{T}\int_T (\dot{y}^2 + \dot{x}^2) dt}}. \quad (19)$$

A positive excitation coefficient means, on average, the energy transfers from fluid to structure and hence excites the structural vibration, while a negative excitation coefficient indicates that the structural motion is damped. The regions corresponding to the positive excitation coefficient are designated as power-in regions, while those with the negative excitation coefficient are refer to as power-out regions.

The spanwise distributions of C_e, $C_{e,y}$ and $C_{e,x}$ at uniform flow velocities of $V = 0.5$ m/s and 1.5 m/s are presented in Fig.19 and Fig.20. At both flow velocities, Model A predicts the variation of the excitation coefficients along the span in a pattern that is different from those for Models B and C. For flow velocity $V = 0.5$ m/s, as can be seen in Fig.19(a), the cross-flow and in-line excitation coefficients share a common power-in region at the middle of the riser between $p/L = 0.4$ and $p/L = 0.6$, according to Model A. Beyond this region, the energy transfer in the two directions seems to be opposite at most locations along the span; i.e. within the region where the riser motion is excited by the fluid forces in the cross-flow direction, it is damped out in the in-line direction and vice versa. The same phenomena are observed and seem to be more perceptible for Models B and C, as illustrated in Figs.19(b) and (c), where the signs of $C_{e,x}$ and $C_{e,y}$ are opposite to each other over almost the entire span of the riser. The predictions of the cross-flow excitation coefficient according to Models B and C are almost exact, while the in-line excitation coefficient predicted by Model B is significantly larger than that by Model C. At flow

velocity $V = 1.5$ m/s, it has previously been shown that the structural response, predicted by Model A, is characterised by travelling waves that propagate in the direction from $p/L = 0$ towards $p/L = 1$. As a consequence, the general power-in region is expected to be located over the span that is close to $p/L = 0$, while the power-out region is expected to be close to the other end. This is verified in Fig.20(a), which illustrates that the excitation coefficient C_e remains positive over approximately the first half span of the riser and becomes alternatively positive and negative over the rest. For Models B and C, in general, the spanwise variation of the excitation coefficient at flow velocity $V = 1.5$ m/s is similar to that at $V = 0.5$ m/s, except that at $V = 1.5$ m/s, the value of the positive C_e is lightly larger over the span close to $p/L = 1$. This is consistent with the insignificant underlying travelling character of the structural response (corresponding to the travelling wave oriented from $p/L = 1$ towards $p/L = 0$).

To study the relationship between the energy transfer and structural motions, the power-in regions, indicated by grey areas, are portrayed together with the magnitude of cross-flow complex mode $|\mathbf{Y}|$ as well as the phase difference ϕ_{xy} in Fig.21 and Fig.22 for a uniform flow at $V = 0.5$ m/s and $V = 1.5$ m/s. As can be seen in Fig.21(a) and Fig.22(a), no clear relation is observed between the energy transfer and the cross-flow motion for Model A. Nevertheless, it is interesting to note that according to Model A, the large amplitude of cross-flow vibration does not necessarily correspond to the power-out region. For example, in Fig.21(a), although the cross-flow vibration is at its maximum around $p/L = 0.5$, the location is associated with the energy flow into the structure. The same phenomenon is observed in experiments by [4]. Furthermore, the underlying mechanism is believed to be related to the effect of the coupled cross-flow and in-line motions on the wake dynamics. This reflects the shortcomings of most existing models, including Models B and C presented here, in the prediction of the coupled cross-flow and in-line VIV. When dealing with the two degrees of freedom VIV, the cross-flow vibration is conventionally treated separately, and the force data obtained from the forced cross-flow vibration are normally used. Therefore the most existing models always predict the power-out region at the location of a large cross-flow vibration. This can be verified by the energy transfer predicted by Models B and C, as presented in Fig.21(b,c) and Fig.22(b,c), which show clearly that the energy is primarily damped out from the structure at locations corresponding to large cross-flow vibrations. Apart from the power-out regions corresponding to large cross-flow vibrations, the energy is also found
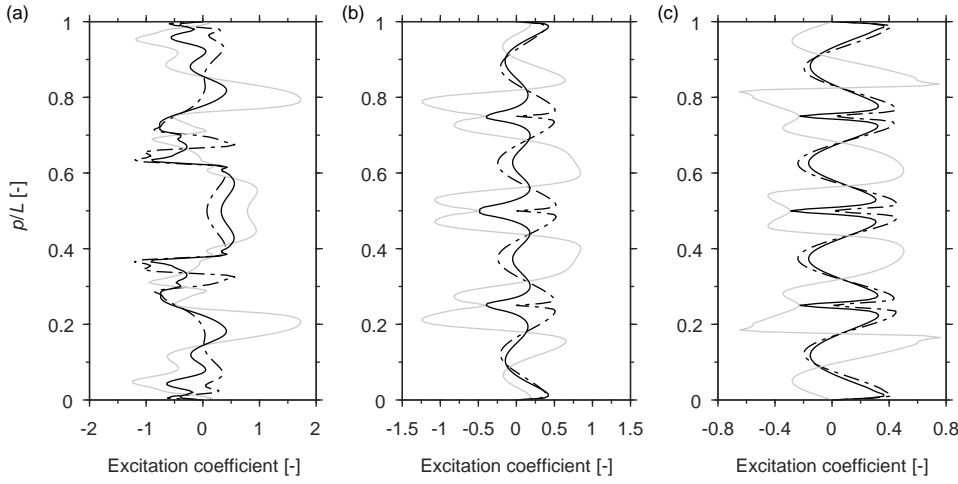
Fig. 19: Force coefficients in phase with velocity along the riser for uniform flow at $V = 0.5$ m/s: (a) results of Model A, (b) results of Model B and (c) results of Model C. Black solid lines represent total excitation coefficient C_e, and black dashed lines and grey solid lines represent $C_{e,y}$ and $C_{e,x}$ respectively
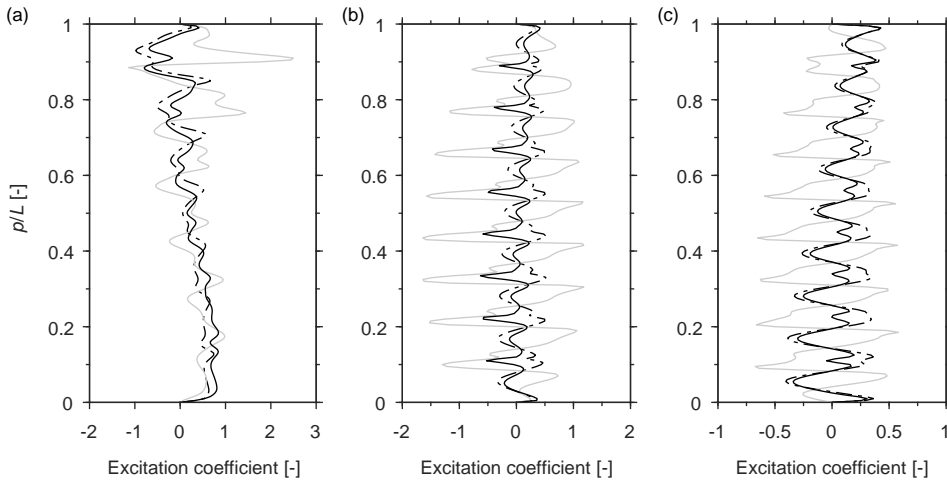

Fig. 20: Force coefficients in phase with velocity along the riser for uniform flow at $V = 1.5$ m/s: (a) results of Model A, (b) results of Model B and (c) results of Model C. Black solid lines represent total excitation coefficient C_e, and black dashed lines and grey solid lines represent $C_{e,y}$ and $C_{e,x}$ respectively
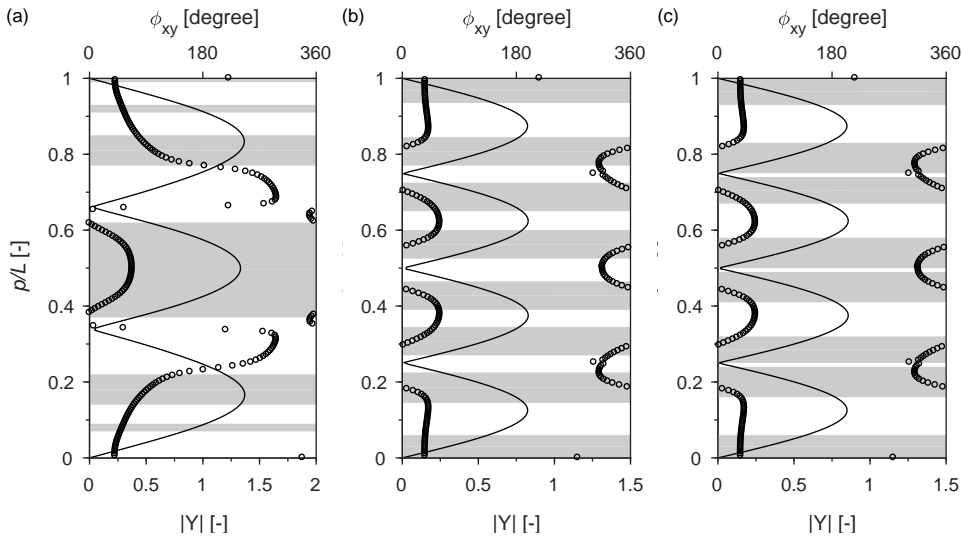

Fig. 21: Power-in regions identified from C_e in comparison with the amplitudes of the cross-flow complex modes $|\mathbf{Y}|$ and phase difference ϕ_{xy} at uniform flow velocity $V = 0.5$ m/s: (a) results of Model A, (b) results of Model B and (c) results of Model C. Power-in regions are indicated by grey colored area. Black solid lines represent $|\mathbf{Y}|$ and circles represent ϕ_{xy}.

Fig. 22: Power-in regions i-
dentified from C_e in com-
parison with the amplitudes
of the cross-flow complex
modes $|\mathbf{Y}|$ and phase differ-
ence ϕ_{xy} at uniform flow ve-
locity $V = 1.5$ m/s: (a) result-
s of Model A, (b) result-
s of Model B and (c) results
of Model C. Power-in regions
are indicated by grey colored
area. Black solid lines repre-
sent $|\mathbf{Y}|$ and circles represent
ϕ_{xy}
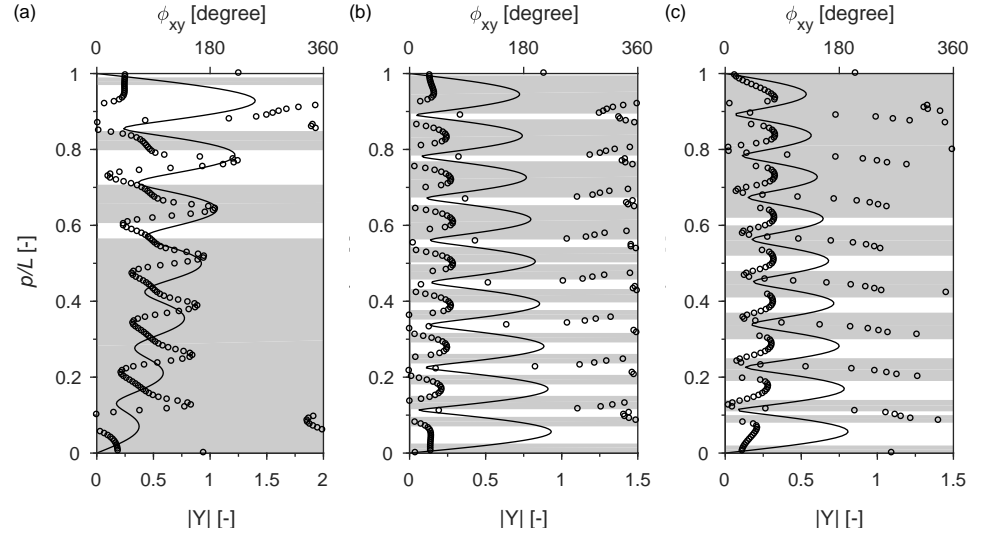
to be damped out from the structure at locations of s-
mall cross-flow vibrations, according to Models B and
C. For example, in Figs.21(b) and (c), the segments of
the riser around the nodes of cross-flow displacemen-
t are associated with power-out regions. Looking into
the contributions to the energy transfer from the cross-
flow and in-line excitation coefficients, as illustrated in
Figs.19(b) and (c), although the cross-flow excitation
coefficients around the location of the nodes are almost
zero, it is the negative in-line excitation coefficients that
make the total energy transfer at these locations nega-
tive.

Concerning the phase difference, no obvious rela-
tion is observed between it and the power-in regions for
Models B and C, since the energy transfer is primarily
determined by the amplitude of cross-flow vibration for
these two cases. For Model A, although no solid trend is
observed, it seems that the power-in regions are mostly
associated with the phase difference that correspond-
s to the counter-clockwise trajectory (between 0° and
180°).

The excitation coefficients for cases of a sheared flow
profile with maximum flow velocity $V = 1.5$ m/s are p-
resented in Fig.23. As can be seen in this figure, for all
three models, the regions of positive C_e are located in
the high-velocity zone, while in the low-velocity region,
the C_e remains negative. The cross-flow and in-line ex-
citation coefficients have the same distribution pattern
as that of C_e and both make significant contribution-
s to the total energy transfer within the high-velocity
region, while in the low-velocity region, the in-line ex-
citation coefficients are small. Fig.23 also displays the
limit, indicated by a horizontal dashed line, between
the power-in and power-out regions. Model A predicts
a wider power-in region $p/L = 0$–0.38 compared to that,

around $p/L = 0-0.28$, predicted by Models B and C.
Different from the uniform flow cases, the energy trans-
fer between the fluid and structure in the sheared flow
cases is normally expected to be determined by the re-
duced velocity. The reduced velocity range of $5 - 7$ is
commonly assumed to be associated with the power-in
region. Here, for Model A, the power-in region corre-
sponds to the reduced velocity range of $U_r = 3.83$–6.15,
and that for Models B and C corresponds to the range
of $U_r = 4.46-6.25$.

The excitation coefficient for the case of sheared flow
with maximum flow velocity $V = 2.5$ m/s is shown in
Fig.24. The distributions of C_e and its cross-flow and
in-line components $C_{e,y}$ and $C_{e,x}$ exhibit the same pat-
tern and trend as those at $V = 1.5$ m/s; therefore, they
are not discussed in detail here. The reduced velocity
is calculated based on the primary dominant cross-flow
frequency, and the range that corresponds to the power-
in region is found to be $U_r = 3.86-6.14$ for Model A
and $U_r = 4.48-6.14$ for Models B and C. These ranges
are similar to those at $V = 1.5$ m/s and suggest that for
all three models, in the sheared flow cases, the power-in
regions are primarily affected by the reduced velocity.
Different from the case of $V = 1.5$ m/s, the structural
response at $V = 2.5$ m/s contains multiple frequen-
cy components, which implies the presence of several
power-in regions that correspond to different frequency
contents. Therefore, a frequency decomposition of $C_{e,y}$
and $C_{e,x}$ based on a Fourier transform is performed.
The contributions from different frequency components
to the cross-flow and in-line excitation coefficients are
calculated with the following equations:

$$W_x(f) = \frac{\mathrm{Re}\left(\mathcal{F}[C_x(t)]\,\overline{\mathcal{F}[\dot{x}(t)]}\right)}{|\mathcal{F}[\dot{x}(t)]|} \qquad (20)$$
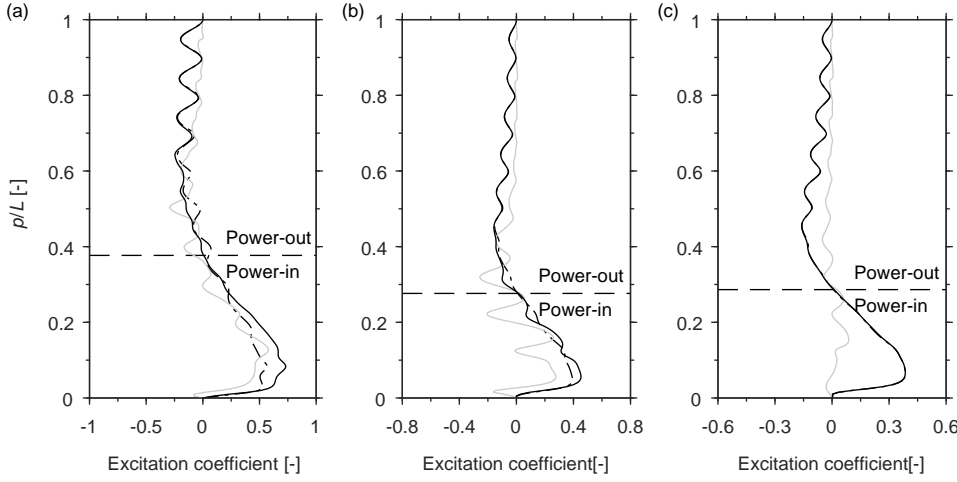
Fig. 23: Force coefficient in phase with velocity along the riser for sheared flow with maximum velocity $V = 1.5$ m/s: (a) results of Model A, (b) results of Model B and (c) results of Model C. Black solid lines represent total excitation coefficient C_e, and black dashed lines and grey solid lines represent $C_{e,y}$ and $C_{e,x}$ respectively
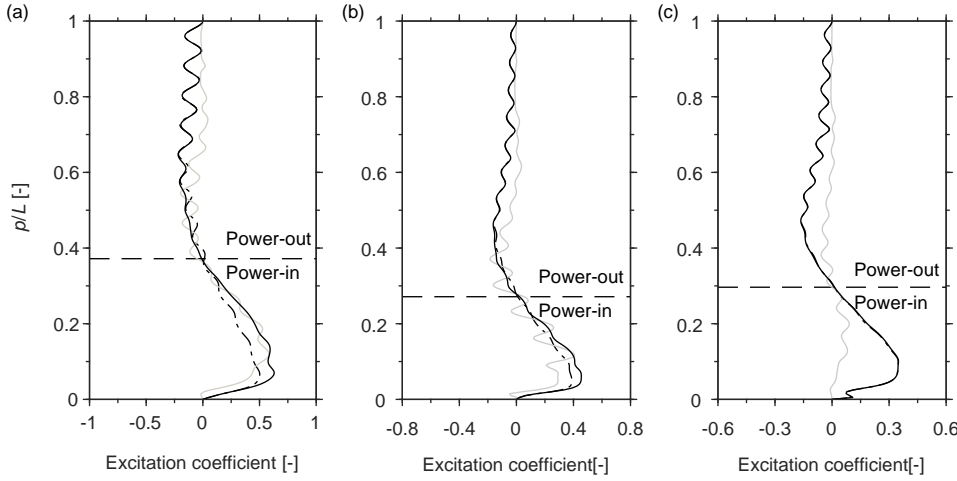

Fig. 24: Force coefficients in phase with velocity along the riser for sheared flow with maximum velocity $V = 2.5$ m/s: (a) results of Model A; (b) results of Model B and (c) results of Model C. Black solid lines represent total excitation coefficient C_e; black dash lines and grey solid lines represent $C_{e,y}$ and $C_{e,x}$ respectively

and

$$W_y\left(f\right) = \frac{\mathrm{Re}\left(\mathcal{F}\left[C_y\left(t\right)\right]\overline{\mathcal{F}\left[\dot{y}\left(t\right)\right]}\right)}{\left|\mathcal{F}\left[\dot{y}\left(t\right)\right]\right|} \quad (21)$$

where $\mathcal{F}\left[\cdot\right]$ denotes Fourier transform and the overline denotes the complex conjugation.

The frequency decomposition of the cross-flow and in-line excitation coefficients are presented in Fig.25 and Fig.26 for all three models. The previously identified dominant frequencies are indicated by arrows. In the cross-flow direction, as illustrated in Fig.25, the frequency decomposition of $C_{e,y}$ does not display obvious differences among the models. For all three models, the most significant positive energy transfer occurs at the main dominant frequency over the same power-in region identified from the total excitation coefficients. Apart from the main power-in region, another region corresponding to a positive $C_{e,y}$ is observed in the low-velocity region around $p/L = 0.7$ close to secondary dominant frequency. It has previously been shown in

Fig.9 that the cross-flow response exhibits two frequency peaks around the secondary dominant frequency. Therefore, in Fig.25, it is not surprising that the positive energy transfer occurs at two distinct frequencies. However, it seems that these two frequencies are well separated for Models B and C, while they are closely spaced for Model A. Concerning the frequency decomposition of the in-line excitation coefficient, similar to the cross-flow case, apart from the strong positive $C_{e,x}$ that occurs at the main dominant frequency, all three models predict another positive energy transfer at the secondary dominant frequency. Different from Models B and C, for which the positive energy transfer at the secondary dominant frequency is mainly located in the low-velocity zone around $p/L = 0.7$, a significant positive $C_{e,x}$ is observed at different locations along the riser for Model A, even in the high-velocity zone, for example at $p/L \approx 0.15$. The difference is believed to be related to the in-line coupling term in the wake oscillator equation. However, further analysis is needed to understand the underlying mechanism. In the in-line

Fig. 25: Frequency decomposition of the cross-flow excitation coefficient for (a) results of Model A, (b) results of Model B and (c) results of Model C.
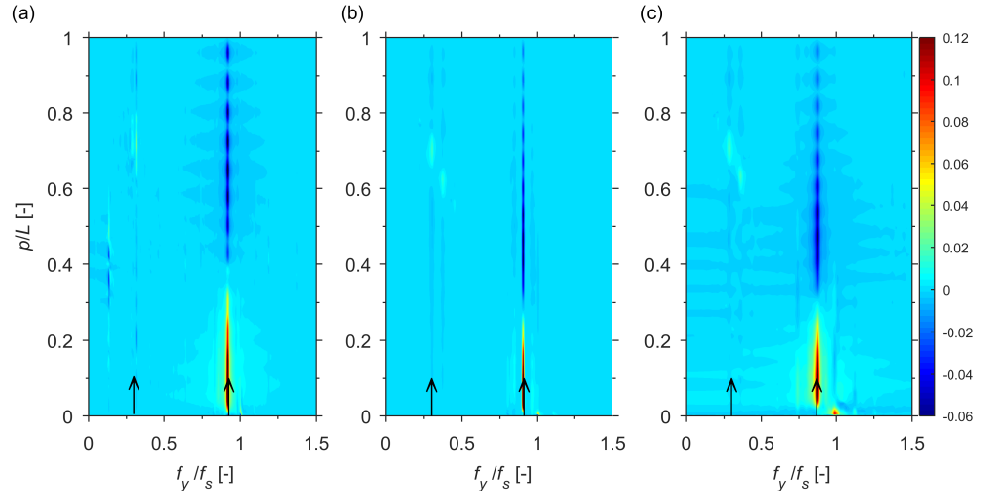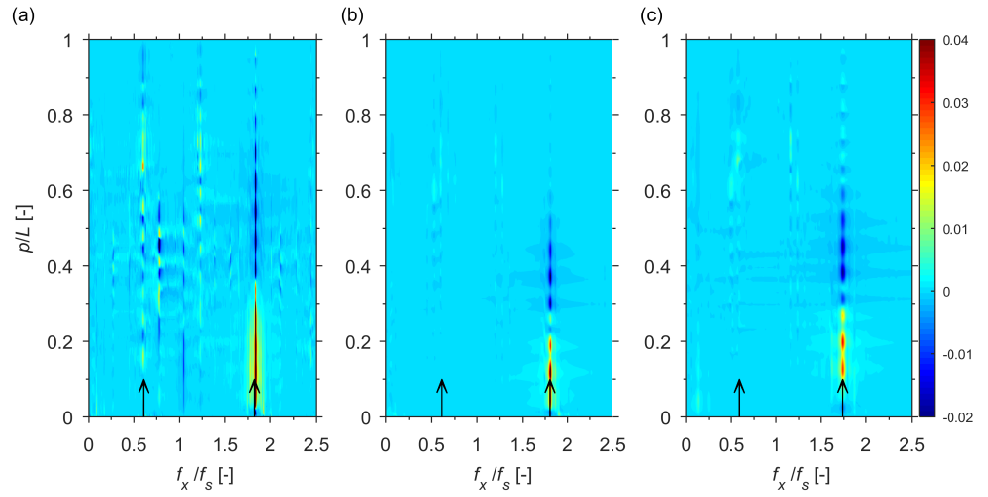

Fig. 26: Frequency decomposition of the in-line excitation coefficient for (a) results of Model A, (b) results of Model B and (c) results of Model C.

direction, apart from the positive energy transfer that occurs at the main and secondary dominant frequencies, a positive $C_{e,x}$ is also observed at a frequency that is approximately twice that of the secondary dominant frequency as a result of the contribution from higher harmonics.

6 Fatigue damage

In this section, a fatigue analysis is conducted for the simulation results obtained from the three models. The main purpose is to investigate the higher harmonics and their contributions to fatigue damage. Therefore, the characteristics of the structural response at higher harmonics are presented in the first subsection through the spectra of the strain, and the fatigue damage is calculated and discussed in the second subsection.

6.1 Strain and higher harmonics

To highlight the higher harmonics, the frequency domain analysis is performed in this subsection based on the bending strains at the surface of the riser. The bending strains of cross-flow and in-line deflections are calculated by the following equation:

$$\epsilon_{x,y} = K_{x,y} \frac{D}{2} \tag{22}$$

where subscripts 'x' and 'y' denote the in-line and cross-flow directions respectively, and $K_{x,y}$ is the curvature calculated as the second derivative of the in-line and cross-flow displacement with respect to the axial coordinate using a central finite difference approximation.

The PSD of in-line and cross-flow strains are evaluated along the riser, and its span-averaged value is plotted in Fig.27–30. In these plots, the vibration frequency is normalised by the Strouhal frequency f_s, and the PSD is normalised by its maximum value for the purpose of comparison. The results from Models A, B and C are
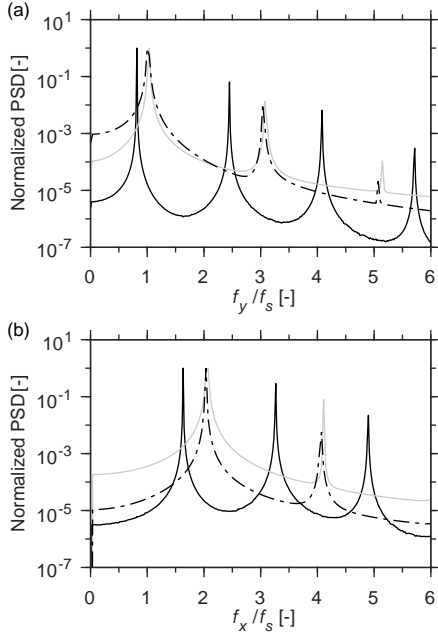
Fig. 27: Spanwise averaged PSD of bending strain due to (a) cross-flow and (b) in-line deflections for uniform flow $V = 0.5$ m/s. Black solid lines represent results from Model A, black dashed lines represent results from Model B and grey solid lines represent results from Model C.
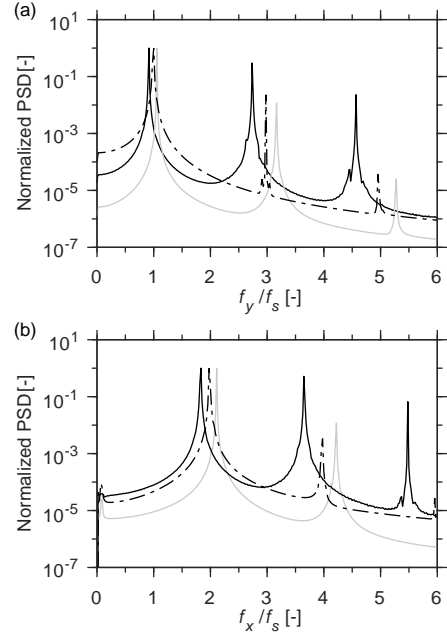

Fig. 28: Spanwise averaged PSD of bending strain due to (a) cross-flow and (b) in-line deflections for uniform flow $V = 1.5$ m/s. Black solid lines represent results from Model A, black dashed lines represent results from Model B and grey solid lines represent results from Model C.

presented in the same plot and indicated by black solid, black dashed and solid grey lines respectively. The spectrum confirms that the in-line response oscillates at a fundamental frequency twice that of the cross-flow response. In addition, the most important observations from these plots are the appearance of higher harmonics. In the cross-flow direction, the riser response is dominated by a strong primary frequency (denoted by $1\times$) and has odd higher harmonics (denoted by $3\times$ and $5\times$), while its even integer multiples (denoted by $2\times$, $4\times$ and $6\times$) are found in the in-line direction.

For the uniform flow cases at $V = 0.5$ m/s and 1.5 m/s, as illustrated in Figs.27 and 28, it is clear that all three models predict distinct frequency peaks at higher harmonics. In general, the comparison of the results from the three models reveals that Model A predicts the most significant components at higher harmonics. The $3\times$ cross-flow response, as reported by [1], is a result of the third harmonic component in the lift force that corresponds to the wake pattern where three vortices are shed. This wake pattern was found to be associated with the large cross-flow vibration when the super-upper branch appears for a small mass ratio system. Since Model A is able to capture this phenomenon of the super-upper branch, see reference [10], it is not surprising that the model predicts the strongest $3\times$ among the three models. Regarding to the $4\times$, $5\times$ and
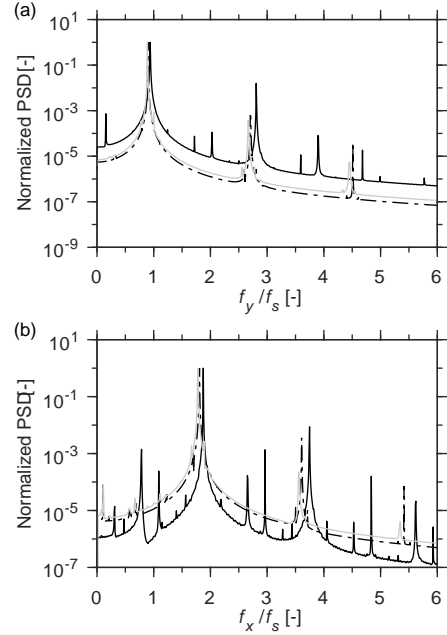

Fig. 29: Spanwise averaged PSD of bending strain due to (a) cross-flow and (b) in-line deflections for sheared flow with maximum velocity $V = 1.5$ m/s. Black solid lines represent results from Model A, black dashed lines represent results from Model B and grey solid lines represent results from Model C.
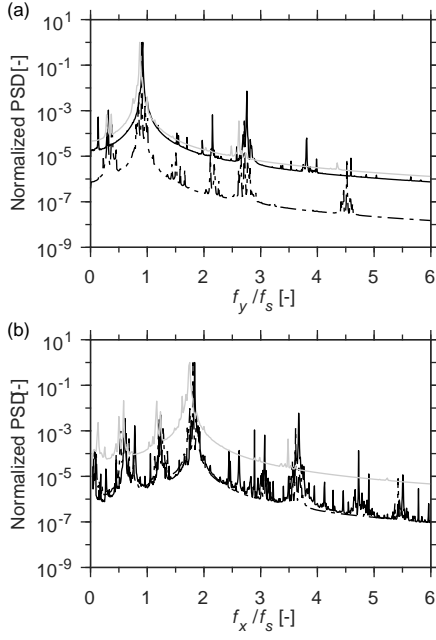
Fig. 30: Spanwise averaged PSD of bending strain due to (a) cross-flow and (b) in-line deflections for sheared flow with maximum velocity $V = 2.5$ m/s. Black solid lines represent results from Model A, black dashed lines represent results from Model B and grey solid lines represent results from Model C.

$6\times$ harmonics, although often observed in the experiments of VIVs of flexible cylinders, little research is conducted on them. It is clear that their contributions are considerable, especially the $4\times$ harmonics, whose magnitude predicted by Model A is comparable to the $2\times$ harmonics.

In Fig.29 and Fig.30, the spanwise averaged PSD of strain for sheared flow cases is presented. It can be seen that at both flow velocities, the frequency spectrum of the strain for Model A is characterised by the richness of the frequency content with small peaks, and this is much more significant compared to that of Models B and C. The relative contributions of higher harmonics are clearly smaller in sheared flow than those in uniform flow. Nevertheless, Model A still predicts the strongest high-harmonic components.

6.2 Fatigue damage rate

In this subsection, the fatigue damage is calculated by applying the Miner summation, and the fatigue damage at a specific location along the riser is given by

$$D_a = \sum_{i=1} \frac{n_i}{N_i} = \frac{1}{a} \sum_{i=1} n_i \left(\Delta\sigma_i\right)^m \qquad (23)$$

where N_i represents the number of cycles to failure at stress range $\Delta\sigma_i$, and n_i denotes the correspond-

ing stress cycles that take place. The number of cycles to failure for a given stress range can be found from an S-N curve, which is associated with the parameters a and m. Here, $\log a = 11.687$ and $m = 3.0$ are taken as suggested by [21]. The rainflow counting method is applied to find n_i for a given time series of strain, and the stress amplitude is obtained by simply multiplying the strain with Young's modulus. It needs to be clarified that the concept of fatigue damage is used loosely here, since in practical applications, the effective stress, such as von Mises stress, should be used in the estimation of fatigue damage. For each simulation result, the fatigue damage is estimated on both the original and a filter version of the signal, where the higher harmonics have been removed and only the primary harmonics ($1\times$ component in the cross-flow and $2\times$ component in the in-line direction) are kept.

In Figs.31 and 32, the distributions of the fatigue damage rate along the riser are presented for the uniform flow cases. It is clear from these figures that while for the cases of Models B and C, the total fatigue damage shows no obvious difference relative to that at the primary frequency, Model A predicts the total fatigue damage to be much higher than its component at the primary frequency. At flow velocity $V = 0.5$ m/s, all three models predict a similar order of maximum damage due to the cross-flow vibrations, as can be seen in Figs.31(a), (c) and (e). For Model A, the excited third mode in the cross-flow vibration leads to a smaller fatigue damage at the primary frequency compared to that of Models B and C for which the cross-flow vibration is dominated by the fourth mode. The significant contributions from higher harmonics make the maximum of the total fatigue damage predicted by Model A comparable to that by Models B and C. In the in-line direction, Model A predicts the highest fatigue damage at the primary frequency, and Model C predicts the least damage. Regarding the total fatigue damage, the significant higher harmonics make the magnitude of total fatigue damage predicted by Model A one order higher than that predicted by Models B and C. At flow velocity $V = 1.5$ m/s, the general trend of differences among the predictions of the three models is similar to those at $V = 0.5$ m/s; therefore, this trend is not discussed in detail here. However, it must be noted that at $V = 1.5$ m/s, the differences between the total fatigue damage and its components at the primary frequency seem to be more significant than at $V = 0.5$ m/s. According to [2], the higher harmonic components in the fluid forces are associated with certain favourable motion trajectories. Therefore, the higher harmonics are naturally expected to be stronger in a travelling wave response, as it allows for these favourable motion trajectories to persist
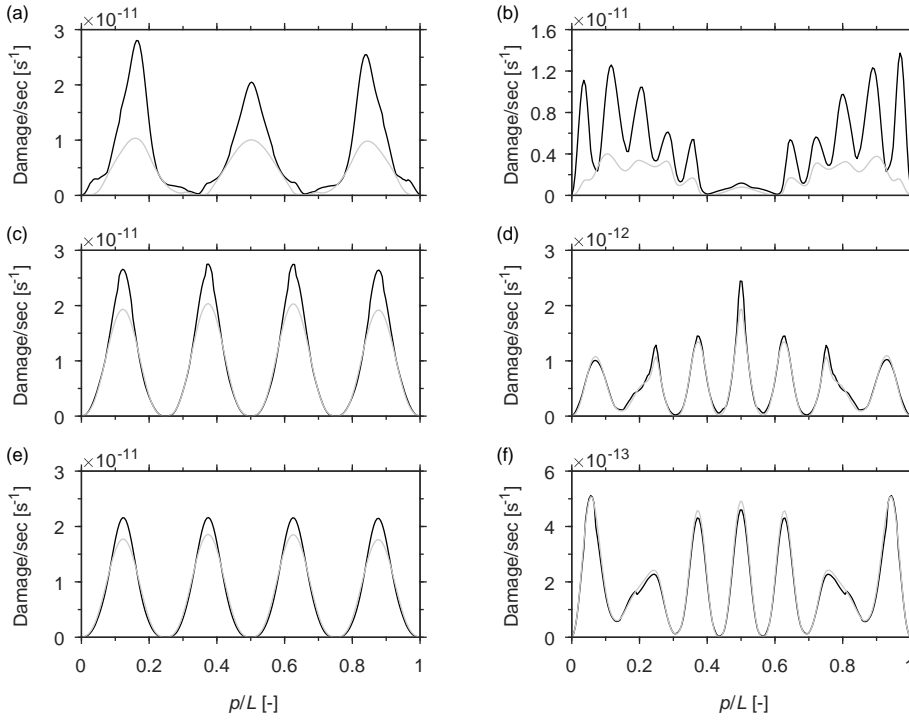
Fig. 31: Predicted fatigue damage rate due to (a,c,e) cross-flow and (b,d,f) in-line deflections at uniform flow $V = 0.5$ m/s for (a,b) Model A, (c,d) Model B and (e,f) Model C. Black solid lines represent the total fatigue damage and grey solid lines represent the fatigue damage estimated from the strain signal after the higher harmonics are removed.
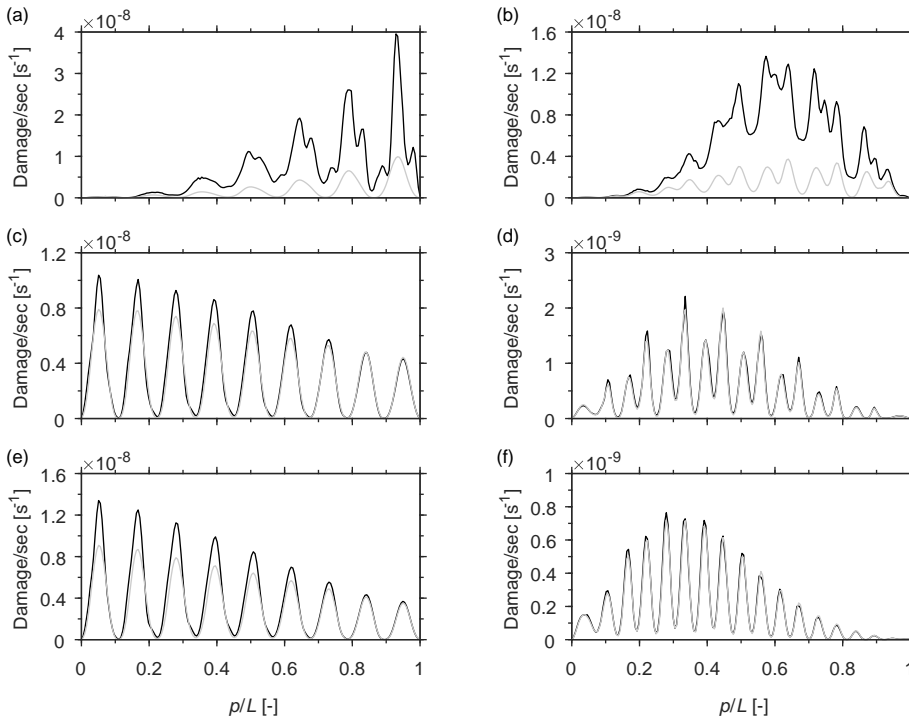

Fig. 32: Predicted fatigue damage rate due to (a,c,e) cross-flow and (b,d,f) in-line deflections at uniform flow $V = 1.5$ m/s for (a,b) Model A, (c,d) Model B and (e,f) Model C. Black solid lines represent the total fatigue damage and grey solid lines represent the fatigue damage estimated from the strain signal after the higher harmonics are removed.

over substantial lengths of the riser [6]. Recall that at $V = 1.5$ m/s, the structural response in the cross-flow direction is dominated by travelling waves, while that at $V = 0.5$ m/s is standing wave dominated. This may imply that the relation between the higher harmonics and motion trajectories are well captured by Model A. However, more studies are needed to confirm this.

The fatigue damage estimated for the sheared flow cases are presented in Fig.33 and Fig.34. Similar to the uniform flow cases, both Model B and Model C predict that fatigue damage mainly occurs at the primary frequency. For Model A, although the total fatigue damage is observed to be different from its component at the primary frequency, the difference between the two

Fig. 33: Predicted fatigue damage rate due to (a,c,e) cross-flow and (b,d,f) in-line deflections for sheared flow with maximum velocity $V = 1.5$ m/s for (a,b) Model A, (c,d) Model B and (e,f) Model C. Black solid lines represent the total fatigue damage and grey solid lines represent the fatigue damage estimated from the strain signal after the higher harmonics are removed.
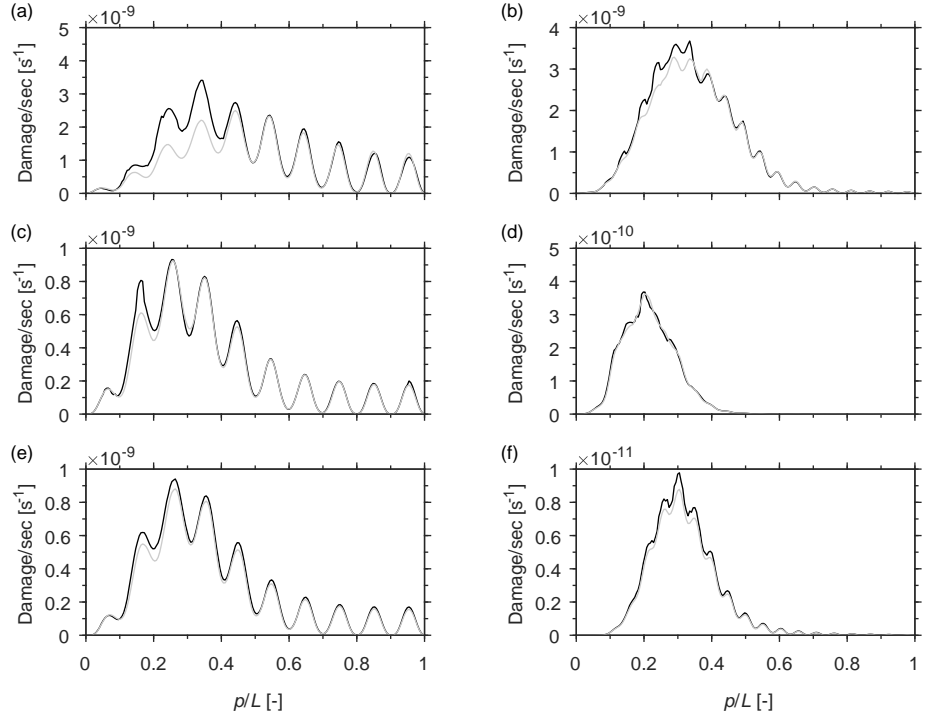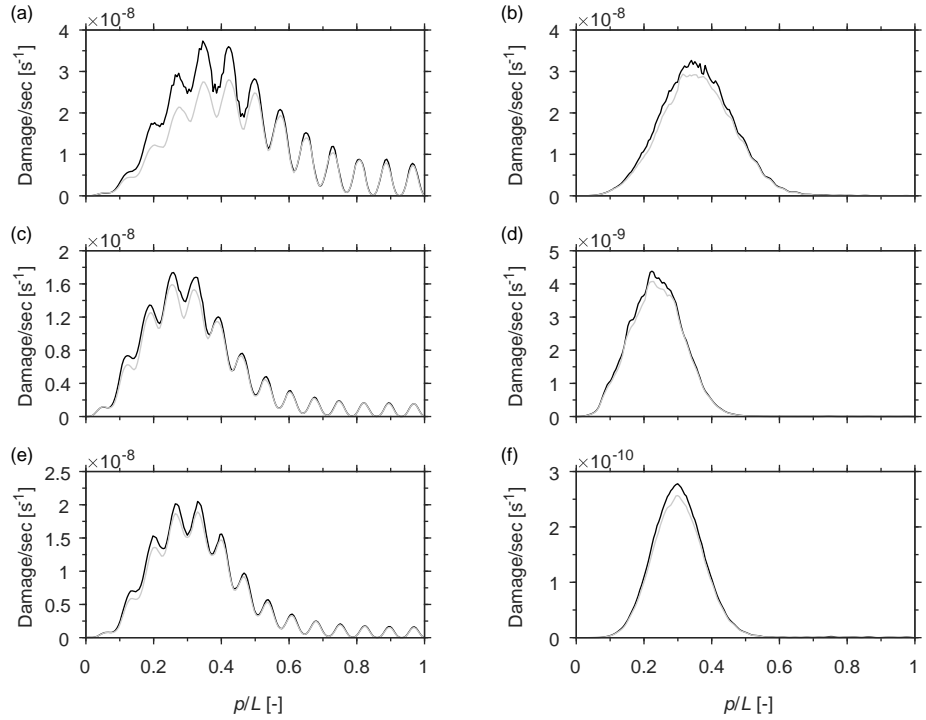

Fig. 34: Predicted fatigue damage rate due to (a,c,e) cross-flow and (b,d,f) in-line deflections for sheared flow with maximum velocity $V = 2.5$ m/s for (a,b) Model A, (c,d) Model B and (e,f) Model C. Black solid lines represent the total fatigue damage and grey solid lines represent the fatigue damage estimated from the strain signal after the higher harmonics are removed.

is much less significant than in the uniform flow cases. This implies that the contribution of higher harmonics in the sheared flow cases may not be as high as those in the uniform flow. Nevertheless, in sheared flow cases, Model A still predicts the highest level of fatigue damage among the three in both cross-flow and in-line directions. While the fatigue damage due to the cross-flow vibrations is approximately the same according to Models B and C, the fatigue caused by in-line vibration for Model C is one order of magnitude smaller than in Model B.

7 Conclusions

In this paper, three different wake oscillator models are used for simulations of VIVs of flexible cylinders subjected to both uniform and linearly sheared flows. The three models differ from each other with respect to the inclusion of the in-line coupling that consists of an in-line motion coupling term and a lift-coupled fluctuating in-line force term. Model A is the most complete model, and Model B excludes the in-line motion coupling term and is similar to the model by Bai [13], while Model C excludes both and is the same as the model used by [12].

In the cases of uniform flow, Models B and C predict similar structural responses, except that the amplitude of in-line vibration predicted by Model C is much smaller than that by Model B. Model A, on the other hand, predicted that the structure would vibrate in a different pattern. Especially at higher flow velocities, according to Models B and C, the structural response in the cross-flow direction is dominated by a standing wave that, according to Model A, has a tendency to vibrate in the form of a travelling wave. For sheared flow cases, no obvious difference was observed regarding the response pattern. All three models predicted the structural response to be dominated by the travelling wave that propagates from a high-velocity to a low-velocity region.

For the uniform flow cases, it has been shown that the energy transfer between the fluid and structure according to Models B and C is primarily determined by the amplitude of cross-flow vibration. In principal, for Models B and C, a positive energy transfer has been identified at locations corresponding to small cross-flow vibrations, while a negative energy transfer occurs when the amplitude of cross-flow vibration exceeds certain values. Such a dependency is not observed in the results of Model A. Instead, it seems that for Model A, the positive energy transfer is mostly associated with a counter-clockwise motion trajectory, which is consistent with experimental observations. For the sheared flow cases, the energy transfer is found to mainly depend on the reduced velocity, and Model A predicts the power-in region corresponding to a wider range of reduced velocities compared to Models B and C.

Finally, the fatigue damage predicted by the three models has been investigated. It has been demonstrated that in the cases of uniform flow, Model A predicts highly significant contributions to the fatigue from higher harmonics, which resulted in a much higher rate of fatigue damage compared to the rates predicted by Models B and C. In the cases of sheared flow, although Model A's predicted fatigue that is caused by higher

harmonics was not as significant as that in the uniform flow cases, Model A still predicts the highest level of fatigue damage among the three. This finding suggests that for a VIV model that does not consider the effect of in-line motions on the wake dynamics, the fatigue damage can be significantly underestimated, and the results therefore need to be taken carefully.

To conclude, the present study highlights the importance of the in-line coupling on the proper modelling of coupled cross-flow and in-line VIVs of flexible cylindrical structures. Both the in-line motion coupling term and the lift-coupled in-line force term are essential and dispensable in the formulation of this in-line coupling. Excluding both, like the model used in [12], or only taking the fluctuating in-line force into account, like the model in [13], would not be able to capture the influence of the motion trajectory and consequently underestimate contributions to the fatigue damage from higher harmonics.

Conflict of interest

The authors declare that they have no conflict of interest.

References

1. Jauvtis, N. and Williamson, C. H. K.: The effect of two degrees of freedom on vortex-induced vibration at low mass and damping, Journal of Fluid Mechanics. 509, 23-62 (2004)
2. Dahl, J. M.,Hover, F. S., Triantafyllou,M. S., Dong, S., and Karniadakis, G. E.: Resonant vibrations of bluff bodies cause multivortex shedding and high frequency forces, Physical review letters. 99(14), 144503 (2007)
3. Wu, J., Lie, H., Larsen, C.M., Liapis, S., Baarholm, R.: Vortex-induced vibration of a flexible cylinder: Interaction of the in-line and cross-flow responses, Journal of Fluids and Structures. 63, 238-258 (2016)
4. Song, L., Fu, S., Cao, J., Ma, L., Wu, J.: An investigation into the hydrodynamics of a flexible riser undergoing vortex-induced vibration, Journal of Fluids and Structures. 63, 325-350 (2016)
5. Song, L., Fu, S., Ren, T., Lu, Z.: Phase Angles of the Vibrations and Hydrodynamic Forces of the Flexible Risers Undergoing Vortex-Induced Vibration, ASME. J. Offshore Mech. Arct. Eng. 139(3), 031803 (2017)
6. Vandiver, J.K., Jaiswal, V., Jhingran, V.: Insights on vortex-induced, traveling waves on long risers, Journal of Fluids and Structures. 25(4), 641-653 (2009)
7. Dahl, J.M.: Vortex-induced vibration of a circular cylinder with combined in-line and cross-flow motion.

PhD thesis, Massachusetts Institute of Technology, MA (2008)

8. Srinil, N. and Zanganeh, H.: Modelling of coupled cross-flow/in-line vortex-induced vibrations using double duffing and van der pol oscillators, Ocean Engineering. 53, 83-97 (2012)

9. Postnikov, A., Pavlovskaia, E., and Wiercigroch, M.: 2DOF CFD calibrated wake oscillator model to investigate vortex-induced vibrations, International Journal of Mechanical Sciences. 127(Supplement C), 176-190 (2017)

10. Qu, Y., Metrikine, A.: A single van der pol wake oscillator model for coupled cross-flow and in-line vortex-induced vibrations, Ocean Engineering. 196, 106732 (2020)

11. Facchinetti, M., de Langre, E., and Biolley, F.: Coupling of structure and wake oscillators in vortex-induced vibrations, Journal of Fluids and Structures. 19, 123-140 (2004)

12. Mina, A.: Modeling the vortex-induced vibrations of a multi-span free standing riser. Master Thesis, Delft University of Technology, Delft (2013)

13. Bai, Xu., Qin, W.: Using vortex strength wake oscillator in modelling of vortex induced vibrations in two degrees of freedom, European Journal of Mechanics - B/Fluids. 48, 165-173 (2014)

14. Ogink, R., Metrikine, A.: A wake oscillator with frequency dependent coupling for the modeling of vortex-induced vibration, Journal of Sound and Vibration. 329, 5452-5473 (2010)

15. Qin, L.: Development of Reduced-Order Models for Lift and Drag on Oscillating Cylinders with Higher-Order Spectral Moments. PhD thesis, Virginia Polytechnic Institute and State University, VA (2004)

16. Lie, H., Henning, B., Jhingran, V.G., Sequeiros, O.E., Kim, V.: Comprehensive Riser VIV Model Tests in Uniform and Sheared Flow, In OMAE2012, 5, 923-930 (2012)

17. Géradin, M., Cardona, A.: Flexible Multibody Dynamics: A Finite Element Approach. Wiley, New York (2001)

18. Chaplin, J.R., Bearman, P.W., Huera-Huarte, F.J., Pattenden, R.: Laboratory measurements of vortex-induced vibrations of a vertical tension riser in a stepped current, Journal of Fluids and Structures. 21(1), 3-24 (2005)

19. Huera-Huarte, F.J.: Multi-mode vortex induced vibration of a flexible circular cylinder. PhD thesis, Imperial College London, London (2004)

20. Bourguet, R., Karniadakis, G., Triantafyllou, M.: Vortex-induced vibrations of a long flexible cylinder in shear flow, Journal of Fluid Mechanics. 677, 342-382 (2011)

21. Trim, A., Braaten, H., Lie, H., and Tognarelli, M.: Experimental investigation of vortex-induced vibration of long marine risers, Journal of Fluids and Structures. 21(3), 335-361 (2005)